PHOTONICS Research

From non-scattering to super-scattering with Mie-tronics

Hooman Barati Sedeh and Natalia M. Litchinitser*

Department of Electrical and Computer Engineering, Duke University, Durham, North Carolina 27708, USA
**Corresponding author: natalia.litchinitser@duke.edu*

Received 14 August 2023; revised 8 October 2023; accepted 8 November 2023; posted 9 November 2023 (Doc. ID 503182); published 13 March 2024

Electric anapoles, arising from the destructive interference of primitive and toroidal electric dipole moments, have recently emerged as a fundamental class of non-scattering sources. On the other hand, super-scattering states represent the opposite regime wherein the scattering cross-section of a subwavelength particle exceeds the single-channel limit, leading to a strong scattering behavior. Here, we demonstrate that the interplay between the topology of light and the subwavelength scatterer can lead to these two opposite responses within an isolated all-dielectric meta-atom. In particular, we present the emergence of a new non-scattering state, referred to as hybrid anapole, which surpasses conventional electric dipole anapoles by achieving a remarkable 23-fold enhancement in the suppression of far-field radiation and almost threefold enhancement in the confinement of electromagnetic energy inside the meta-atom. We also explore the role of particle orientation and its inversion symmetry in the scattering response and predict the possibility of switching between non-scattering and super-scattering states within the same platform. The presented study elucidates the role of light and matter topologies in the scattering response of subwavelength meta-atoms, uncovering two opposite regimes of light-matter interaction and opening new avenues in applications such as nonlinear optics and spectroscopy.

https://doi.org/10.1364/PRJ.503182

1. INTRODUCTION

Before the proposal of Bohr's model, in the early days of electron discovery, several models, such as non-radiating sources that do not radiate energy into the far-field, had been considered to explain the atomic structure and address the paradox of unstable atoms [1–3]. While Bohr eventually addressed this problem, the idea of non-radiating sources extended to other branches of science, such as the physics of elementary particles, quantum field theory, nuclear science, and astrophysics [4–12]. Despite considerable efforts, only recently an optical non-radiating state, known as anapole (from Greek "ana," "without," thus meaning "without poles"), has been experimentally demonstrated in high refractive index engineered dielectric nanoparticles, known as meta-atoms [13–19]. In particular, contrary to the plasmonics nanoparticles, all-dielectric scatterers, and their two-dimensional (2D) periodic arrangements, known as metasurfaces [20–26], provide an alternative, low-loss route to light-matter interaction at the nanoscale and have enabled various remarkable phenomena and applications, including Kerker, anti-Kerker, transverse Kerker effects [27–33], lattice resonances [34–36], beam steering [37–39], holography [40–42], invisibility cloaking [43–46], optical force manipulation [47–50], absorption engineering [51–54], and nonlinear harmonic generation [55–60].

The multipole decomposition of electromagnetic fields can characterize light interactions with all-dielectric nanostructures [29]. In particular, such a theoretical framework provides an opportunity to introduce the so-called toroidal contributions [61–65], enabling a platform to achieve unprecedented optical phenomena such as the formation of non-scattering anapole [15–19,66–68] and super-scattering [69–74] states, which are two opposite extreme regimes of light-matter interactions. In the scattering cross-section (SCR) spectra, each multipole corresponds to an independent scattering channel with an upper bound known as the single-channel limit, which is defined by $(2l+1)\lambda^2/2\pi$, wherein l represents the order of the multipole. However, the constructive interference of at least two resonant modes can surpass this limit resulting in a phenomenon of super-scattering, and enabling a plethora of applications, including solar cells and sensing [75–78], to name a few. Contrary to the super-scattering regime, anapole states form as a result of the destructive interference between primitive moments and their toroidal contributions [13–19]. Vanishing scattering accompanied by strong energy confinement in high-index dielectric meta-atoms supporting electric dipole anapole (EDA) states has recently attracted much research interest in the areas of strong exciton coupling [79,80], second- and third-harmonic generation [81–85], Raman

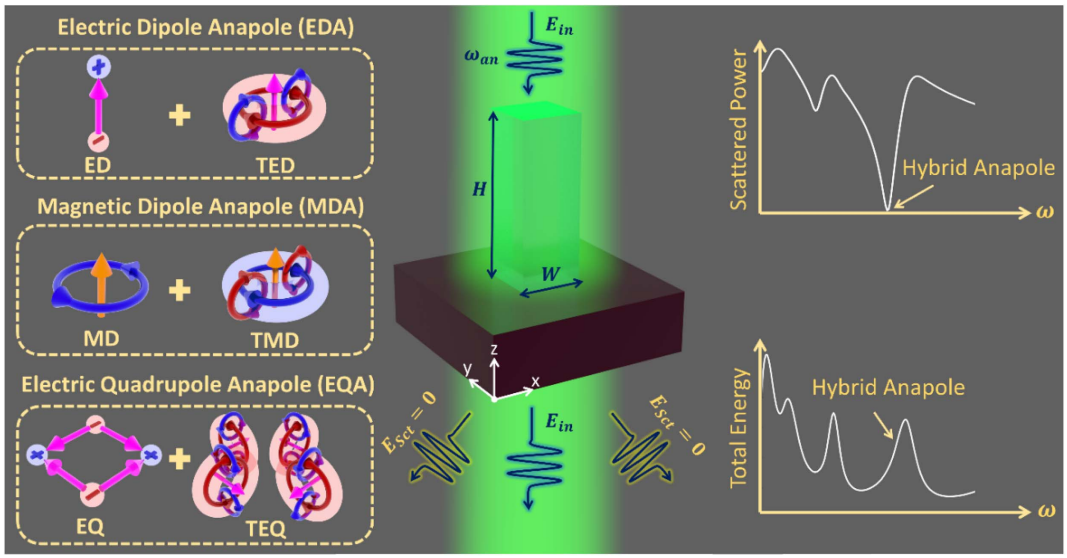

Fig. 1. Schematic representation of the formation of a hybrid anapole state within an all-dielectric cuboid meta-atom with the width and height of $W = 295$ nm and $H = 466$ nm, respectively. A monochromatic plane wave that is polarized along the x axis impinges on the meta-atom along the z axis and excites complex displacement current configurations, leading to the suppression of the far-field scattering and significant energy confinement. Inset depicts the primitive and toroidal contributions up to the electric quadrupole term with red and blue colors demonstrating the magnetic and electric field distributions, respectively.

scattering [86,87], photothermal effect [88], energy guiding [89,90], and lasing [91]. While to date, most of the works in this field of research are limited to the studies of EDAs, other types of nonradiative states, such as magnetic dipole anapole (MDA) and electric and magnetic quadrupole anapoles (EQA and MQA, respectively) remain largely unexplored. However, such higher-order anapole states can enhance radiation suppression and confinement of electromagnetic energy if designed to spectrally overlap with the corresponding dipolar moments [92]. The intriguing potential of non-scattering regimes—resulting from the simultaneous destructive interference of electric and magnetic Cartesian multipoles with their toroidal contributions—has garnered attention in several studies in recent years [92–97]. Notably, the experimental observation of the hybrid anapole (HA) was recently achieved in the seminal work by Valero *et al.* [94], intensifying interest in this distinctive regime of light-matter interaction. Here, we demonstrate the design of polycrystalline silicon cuboid meta-atoms that support higher-order non-radiative states up to electric quadrupole anapole order at a given wavelength, leading to a notable suppression of far-field radiation and a remarkable 20-fold enhancement of electromagnetic energy confinement within the subwavelength meta-atom as it is schematically shown in Fig. 1. We also demonstrate that, depending on the orientation of the scatterer, its optical response can be tuned from non-radiative to radiative resonant modes. Moreover, we reveal that breaking the out-of-plane inversion symmetry of the meta-atom from a cuboid to a pyramid provides an opportunity for achieving a strong super-scattering optical response, with a 130% enhancement in scattering behavior. The presented concept can open new prospects for enhancing nonlinear conversion efficiency, remote sensing, and optical communications in scattering media.

2. UNDERLYING PHYSICS OF HYBRID ANAPOLES

The optical response of nonmagnetic meta-atoms can be described using the multipole expansion approach, which can be performed using either a spherical or Cartesian basis [98–102]. The former is based on the multipole decomposition of electromagnetic fields in terms of the spherical harmonic coefficients, leading the total scattering cross-section to be defined as a series of coefficients as $\sigma_{\mathrm{Sct}}(\omega) = \frac{\pi}{k^2}\sum_{l=1}^{\infty}\sum_{m=-l}^{+l}(2l+1)\cdot[|a_E(l,m;\omega)|^2 + |a_M(l,m;\omega)|^2]$, where $a_E(l,m;\omega)$ and $a_M(l,m;\omega)$ represent the spherical electric and magnetic multipole scattering coefficients, respectively [101]. On the other hand, the second approach is based on the multipole decomposition of the Cartesian components of induced current density within the meta-atom as $\boldsymbol{J}_{\mathrm{in}}(\boldsymbol{r};\omega) = \sum_{l=0}\frac{(-1)^l}{l!}\cdot F^{(l)}_{i\ldots k}\partial_i\ldots\partial_k\delta(r)$, with $F^{(l)}_{i\ldots k} = \int_{V_p}\boldsymbol{J}_{\mathrm{in}}(\boldsymbol{r};\omega)\boldsymbol{r}_i\ldots\boldsymbol{r}_k d\boldsymbol{r}$ denoting a tensor of rank l that corresponds to different Cartesian multipoles [102]. According to the theory of irreducible multipoles, the scattering cross-section of a subwavelength meta-atom can be expressed as (see Appendix A)

$$\begin{aligned}\sigma_{\mathrm{sct}}(\omega) = {} & \frac{k_0^4\sqrt{\epsilon_d}}{12\pi\epsilon_0^2\mu_0 c}\left|\boldsymbol{p} + \frac{ik_0\epsilon_d}{c}\boldsymbol{T}_1^{(e)} + \frac{ik_0^3\epsilon_d^2}{c}\boldsymbol{T}_2^{(e)}\right|^2 \\ & + \frac{k_0^4(\epsilon_d)^{3/2}}{12\pi\epsilon_0 c}\left|\boldsymbol{m} + \frac{ik_0\epsilon_d}{c}\boldsymbol{T}^{(m)}\right|^2 + \frac{k_0^6(\epsilon_d)^{3/2}}{160\pi\epsilon_0^2\mu_0 c} \\ & \times\sum_{u,v}\left|\hat{Q}^{(e)}_{u,v} + \frac{ik_0\epsilon_d}{c}\hat{T}^{(Q_e)}_{u,v}\right|^2 \\ & + \frac{k_0^6(\epsilon_d)^{5/2}}{160\pi\epsilon_0 c}\sum_{u,v}\left|\hat{Q}^{(m)}_{u,v} + \frac{ik_0\epsilon_d}{c}\hat{T}^{(Q_m)}_{u,v}\right|^2, \end{aligned} \tag{1}$$

where $\boldsymbol{p}(\omega)$, $\boldsymbol{m}(\omega)$, $\hat{Q}^{(e)}(\omega)$, and $\hat{Q}^{(m)}(\omega)$ correspond to the primitive multipolar moments of electric and magnetic dipoles and quadrupole tensors (ED, MD, EQ, and MQ, respectively), while $\boldsymbol{T}_1^{(e)}(\omega)$ and $\boldsymbol{T}_2^{(e)}(\omega)$ denote the electric toroidal dipoles (ETD) of the first and second kind, $\boldsymbol{T}^{(m)}(\omega)$ is the toroidal magnetic dipole (TMD), and $\hat{T}^{(Q_e)}(\omega)$ and $\hat{T}^{(Q_m)}(\omega)$ represent the toroidal electric and magnetic quadrupole tensors (TEQ and TMQ, respectively); c is the speed of light in vacuum, ϵ_d is the dielectric constant of the surrounding medium, ϵ_0, μ_0, and k_0 are the permittivity, permeability, and wavenumber in free space, and u and v represent different components of each tensor. Each of the components of the primitive Cartesian multipole moments in Eq. (1) can be expressed in terms of the induced current within the particle as [93]

$$
\begin{aligned}
p_u(\omega) &= \frac{i}{\omega}\int_{V_p} \boldsymbol{J}_{\mathrm{in},u}(\boldsymbol{r}';\omega)\mathrm{d}\boldsymbol{r}',\\
m_u(\omega) &= \frac{1}{2}\int_{V_p} (\boldsymbol{r}'\times\boldsymbol{J}_{\mathrm{in}}(\boldsymbol{r}';\omega))_u\mathrm{d}\boldsymbol{r}',\\
\hat{Q}^{(e)}_{u,v}(\omega) &= \frac{i}{\omega}\int_{V_p} r'_u J_{\mathrm{in},v}(\boldsymbol{r}';\omega) + r'_v J_{\mathrm{in},u}(\boldsymbol{r}';\omega)\\
&\quad -\frac{2}{3}\delta_{uv}(\boldsymbol{r}'\cdot\boldsymbol{J}_{\mathrm{in}}(\boldsymbol{r}';\omega))\mathrm{d}\boldsymbol{r}',\\
\hat{Q}^{(m)}_{u,v}(\omega) &= \frac{1}{3}\int_{V_p} ((\boldsymbol{r}'\times\boldsymbol{J}_{\mathrm{in}}(\boldsymbol{r}';\omega))_u r'_v + (\boldsymbol{r}'\times\boldsymbol{J}_{\mathrm{in}}(\boldsymbol{r}';\omega))_v r'_u)\mathrm{d}\boldsymbol{r}',
\end{aligned}
\tag{2}
$$

where V_p is the volume of the meta-atom, the operators of $\cdot$ and $\times$ represent the scalar and vector products, respectively, and δ_{uv} denotes the Kronecker delta function. In addition to the primitive multipoles, the contribution of the toroidal moments can also be expressed in terms of induced displacement current as

$$
\begin{aligned}
T^{(e)}_{1,u}(\omega) &= \frac{1}{10}\int_{V_p} (\boldsymbol{r}'\cdot\boldsymbol{J}_{\mathrm{in}}(\boldsymbol{r}';\omega))r'_u - 2|\boldsymbol{r}'|^2\boldsymbol{J}_{\mathrm{in},u}(\boldsymbol{r}';\omega)\mathrm{d}\boldsymbol{r}',\\
T^{(e)}_{2,u}(\omega) &= \frac{1}{280}\int_{V_p} 3|\boldsymbol{r}'|^4\boldsymbol{J}_{\mathrm{in},u}(\boldsymbol{r}';\omega)\\
&\quad - 2|\boldsymbol{r}'|^2(r'\cdot\boldsymbol{J}_{\mathrm{in}}(\boldsymbol{r}';\omega))r'_u\mathrm{d}\boldsymbol{r}',\\
T^{(m)}_{u}(\omega) &= \frac{i\omega}{20}\int_{V_p} |\boldsymbol{r}'|^2(\boldsymbol{r}'\times\boldsymbol{J}_{\mathrm{in}}(\boldsymbol{r}';\omega))_u\mathrm{d}\boldsymbol{r}',\\
\hat{T}^{(Q_e)}_{uv}(\omega) &= \frac{1}{42}\int_{V_p} (4(\boldsymbol{r}'\cdot\boldsymbol{J}_{\mathrm{in}}(\boldsymbol{r}';\omega))r'_u r'_v\\
&\quad + 2(\boldsymbol{r}'\cdot\boldsymbol{J}_{\mathrm{in}}(\boldsymbol{r}';\omega))|\boldsymbol{r}'|^2\delta_{uv} - 5(r'_u\boldsymbol{J}_{\mathrm{in},v}(\boldsymbol{r}';\omega)\\
&\quad + r'_u\boldsymbol{J}_{\mathrm{in},u}(\boldsymbol{r}';\omega))|\boldsymbol{r}'|^2)\mathrm{d}\boldsymbol{r}',\\
\hat{T}^{(Q_m)}_{uv}(\omega) &= \frac{i\omega}{42}\int_{V_p} |\boldsymbol{r}'|^2((\boldsymbol{r}'\times\boldsymbol{J}_{\mathrm{in}}(\boldsymbol{r}';\omega))_u r'_v\\
&\quad + (\boldsymbol{r}'\times\boldsymbol{J}_{\mathrm{in}}(\boldsymbol{r}';\omega))_v r'_u)\mathrm{d}\boldsymbol{r}'.
\end{aligned}
\tag{3}
$$

As can be seen from Eqs. (1)–(3), the direct consequence of irreducible Cartesian multipole expansion is the possibility of distinguishing higher-order toroidal contribution within the SCR spectrum, thus providing an opportunity to induce various anapole states by satisfying the following conditions:

$$
\begin{aligned}
\text{EDA: } &\boldsymbol{p}(\omega) + \frac{ik_0\epsilon_d}{c}\boldsymbol{T}_1^{(e)}(\omega) = 0,\\
\text{MDA: } &\boldsymbol{m}(\omega) + \frac{ik_0\epsilon_d}{c}\boldsymbol{T}^{(m)}(\omega) = 0,\\
\text{EQA: } &\hat{Q}^{(e)}(\omega) + \frac{ik_0\epsilon_d}{c}\hat{T}^{(Q_e)}(\omega) = 0,\\
\text{MQA: } &\hat{Q}^{(m)}(\omega) + \frac{ik_0\epsilon_d}{c}\hat{T}^{(Q_m)}(\omega) = 0.
\end{aligned}
\tag{4}
$$

Equation (4) provides the conditions for exciting any type of higher order anapole state (up to MQA) at a particular frequency $\omega = \omega_{\mathrm{an}}$. Note that, while the destructive interference between the first and second type of electric toroidal dipole moments $[\boldsymbol{T}_1^{(e)}(\omega) + ik_0^2\epsilon_d\boldsymbol{T}_2^{(e)}(\omega) = 0]$ leads to so-called toroidal anapoles, we are not considering this case here due to the negligible strength of $\boldsymbol{T}_2^{(e)}(\omega)$ (see Appendix B).

3. DYNAMICS OF HYBRID ANAPOLE

The excitation of HAs within a polycrystalline silicon cuboid meta-atom has been studied using the numerical simulations based on the finite-element method (FEM) implemented in the commercial software COMSOL Multiphysics (see Appendix C for details). The cuboid scatterer is assumed to have a square cross-section with a width of W in x and y directions, and a height of H in the z direction, as shown in Fig. 1. To investigate the effect of the geometry of the cuboid meta-atom on its scattering characteristics, first, we fixed the meta-atom width to $W = 295$ nm and changed its height from 300 to 500 nm, while in the second scenario, the height was set to $H = 466$ nm, and the width was changed from 100 to 310 nm over the wavelength range of 850–1150 nm. The contributions of the various multipolar moments were obtained by integrating the displacement current induced within the meta-atom using Eqs. (2) and (3), and their corresponding normalized total scattering cross-sections are shown in Figs. 2(a) and 2(b) in logarithmic scale for the former and latter cases, respectively. As can be seen from these figures, the scattering response of the meta-atom changes significantly as a result of varying the height and width of the meta-atom. In particular, when the height and width of the scatterer change in the range 420 nm $< H <$ 500 nm and 275 nm $< W <$ 310 nm, significant suppression of the peaks in the optical response of the meta-atom can be observed, marked by dashed lines, with the minimum value of $\sigma_{\mathrm{Total}}(\omega)|_{\mathrm{min}} \approx 3\times10^{-4}$ μm^2.

To clarify the physical origin of such a significant suppression of far-field radiation, the contributions of each higher-order multipolar moment (i.e., primitive + toroidal) are plotted in Figs. 2(c) and 2(d) as functions of height and width over the same wavelength range of 850–1150 nm, respectively. As can be seen from these panels, upon varying the geometrical dimensions of the scatterer, several branches of resonances, marked by black dashed lines, emerged within the scattering spectra. In contrast to the optical response of other multipoles, two resonance scatterings can be seen upon varying the dimensions of the meta-atom, which shift toward longer wavelength as both the height and width of the scatterer increase. In particular,

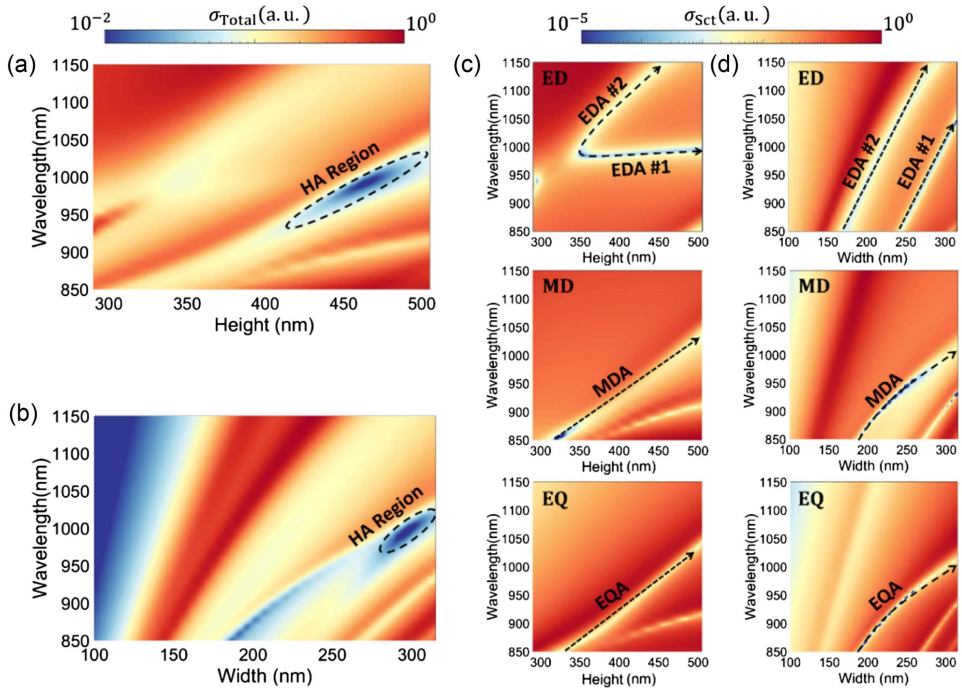

Fig. 2. Normalized total scattering cross-section of the cuboid meta-atom as a function of (a) height and (b) width and an operating wavelength under plane-wave illumination in logarithmic scale. The contribution of ED, MD, and EQ multipolar moments excited in the meta-atom as a function of (c) height and (d) width with respect to wavelength. By changing the topology of the meta-atom, several resonances emerge and disappear at certain spectral positions, leading to the formation of resonant branches that shift toward longer wavelengths as the size of the meta-atom increases.

changing the height of the meta-atom results in the shift of the minima within the MD and EQ spectra, whereas the ED and EQ resonance scatterings shift as the result of varying the width of the meta-atom (see Appendix D for simulation results of MQ). Therefore, by changing the dimensions of the meta-atom, the spectral position of the minima in its scattering spectra can be overlapped at the same operating wavelength, leading to the regions with suppressed radiation, as shown in Figs. 2(a) and 2(b).

Despite the existence of spectral regions with suppressed far-field radiation, such an optical response does not necessarily indicate the excitation of the HA state and the satisfaction of conditions given by Eq. (4). Indeed, the suppression of the far-field radiation pattern may be attributed to the near-zero values of the induced displacement currents within the meta-atom [i.e., $\boldsymbol{J}_{\mathrm{in}}(\boldsymbol{r},\omega)\approx 0$], which yields the simultaneous suppression of both primitive [Eq. (2)] and toroidal [Eq. (3)] moments. However, such an optical behavior differs from the HA response as it does not lead to the confinement of energy within the meta-atom. According to Eq. (4), to excite an anapole state of any type, its corresponding primitive and toroidal contributions should destructively interfere with one another, that is, $I_l=|P+T|^2=|P|^2+|T|^2+2|P||T|\cos(\varphi_P-\varphi_T)\approx 0$, where I_l is the intensity of a particular moment, while P (φ_P) and T (φ_T) denote the amplitude (phase) of its primitive and toroidal contributions, respectively. The intensity of a particular channel vanishes in the far-field, if the following two conditions are simultaneously satisfied: $|P|\approx|T|$ and $\varphi_P-\varphi_T\approx\pm\pi$. To study the origins of the emerged dips within the scattering spectra, we evaluate the explicit contributions of both primitive and toroidal moments as functions of height (400 nm $< H <$ 500 nm) over the wavelength range between 900 and 1200 nm (see Appendix E for the results of the corresponding study of the moments as functions of width). Next, we identify the regions in the parameter space wherein the conditions of inducing anapoles $|P|-|T|\approx 0$ and $\varphi_P-\varphi_T\approx\pm\pi$ are satisfied with respect to the operating wavelength and height of the meta-atom as it is shown in Fig. 3. It should be mentioned that, since the incident electric field is polarized along the x direction, we have only considered the contributing multipoles of p_x, m_y, $\hat{Q}^{(e)}_{xz}$, and $T^{(e)}_{1,x}$, $T^{(m)}_{y}$, $\hat{T}^{(Q_e)}_{xz}$ for primitive and toroidal, respectively.

As can be seen from Figs. 3(a) and 3(b), while several branches of resonances emerge within the amplitude spectra of the ED multipole, the phase difference condition ($\varphi_{p_x}-\varphi_{T_x}\approx\pm\pi$) is only fulfilled for two branches, leading to the excitation of electric dipole anapoles that are red-shifting toward longer wavelength once the height of the meta-atom increases from 400 to 500 nm. On the other hand, despite the fact that individual amplitude and phase conditions for the MD moment occur in the broader spectral range [see Figs. 3(c) and 3(d)], the magnetic dipole anapole is excited in a narrower range compared to its electrical counterpart since both necessary conditions are fulfilled simultaneously in a narrow spectral region. Moreover, the same scattering response as that of the EDA can be found for the electric quadrupole anapole, as shown in Figs. 3(e) and 3(f). In particular, in contrast to the recent study that demonstrated the excitation of HA within all-dielectric scatterer [92], both the amplitude and phase conditions for exciting ideal EQA are satisfied in the spectral range of

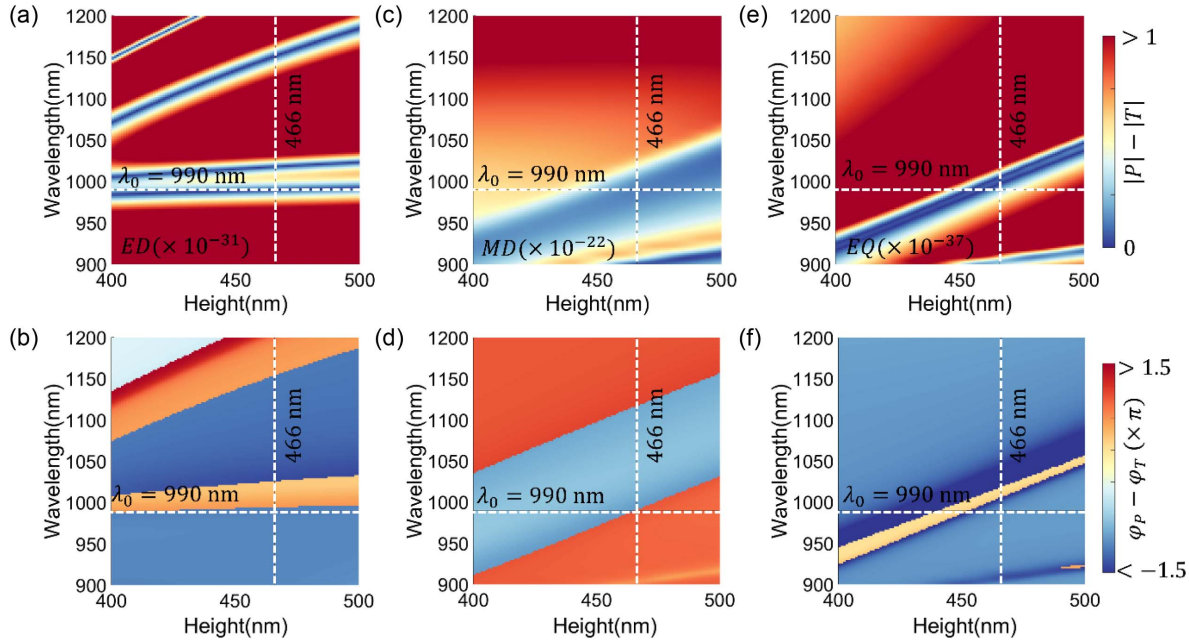

Fig. 3. Explicit contributions of amplitude and phase of primitive and toroidal moments as functions of height and wavelength for (a), (b) ED; (c), (d) MD; and (e), (f) EQ. An anapole of any kind is excited in regions wherein both conditions are simultaneously satisfied. The vertical dashed line corresponds to the dimension at which the HA state can be excited up to the EQA at the operating wavelength of $\lambda = 990$ nm (horizontal dashed line).

interest for the cuboid geometry, making it an appropriate platform for confining electromagnetic energy at the nanoscale. To the best of our knowledge, this is the first prediction of the possibility for exciting an ideal electric quadrupole anapole (both conditions are satisfied exactly as $|\hat{Q}^{(e)}_{xz}| = |\hat{T}^{(Q_e)}_{xz}|$ and $\varphi_{\hat{Q}^{(e)}_{xz}} - \varphi_{\hat{T}^{(Q_e)}_{xz}} = -\pi$) in an all-dielectric subwavelength scatterer. It should be noted that, despite the excitation of three higher-order anapoles in the spectral window of interest, the MQA conditions are not satisfied within this range, which is mainly attributed to the fact that the phase difference between $\hat{M}_{yz}$ and $\hat{T}^{(Q_m)}_{yz}$ is much smaller than π. Nevertheless, for $H < 450$ nm, the MQA is excited, which appears to be the first theoretical observation of such a type of HA (see Appendix D for more details). From Fig. 3, we choose the dimensions of the cuboid meta-atom to be $W = 295$ nm and $H = 466$ nm, shown with a dashed white vertical line, to excite HA states at around $\lambda = 990$ nm (indicated with a horizontal line) up to the electric quadrupole anapole. To explicitly demonstrate the formation of the HA within such a meta-atom, we calculate its optical response with respect to the operating wavelength, as shown in Fig. 4.

Figures 4(a)–4(c) demonstrate the amplitude of the primitive (solid line) and toroidal (dotted curve) contributions together with their relative phase difference up to electric quadrupole multipole as a function of the operating wavelength. As can be seen from these panels, at the operating wavelength of $\lambda = 990$ nm, the general conditions of Eq. (4) are satisfied ($|P| \approx |T|$ and $\angle\varphi_P - \angle\varphi_T \approx \pm\pi$), leading to the formation of an HA state within the meta-atom. In particular, by carefully choosing the dimensions of the cuboid meta-atom, it is possible to excite the anapoles of all the contributing moments in close vicinity of each other, leading to a strong suppression of radiation in the far-field, as shown in Fig. 4(d). Note that, despite the presence of a dip in the spectrum of σ_{MQ}, it does not correspond to the formation of MQA as the condition for the phase of MQA is not satisfied at this wavelength (see Appendix D for more information). In addition, the sum of the contributing moments $[\sigma_{\mathrm{Sum}}(\omega) = \sigma_{\mathrm{ED}} + \sigma_{\mathrm{MD}} + \sigma_{\mathrm{EQ}} + \sigma_{\mathrm{MQ}}]$ and the total scattering cross-section directly computed from COMSOL are in excellent agreement, proving that only the first four multipoles (up to MQ) are sufficient for explaining the optical response of the cuboid meta-atom. The energy confinement at different spectral positions within the scattering spectra of the meta-atom is also shown in Fig. 4(e). For this purpose, we evaluated the total electromagnetic energy, $w_T = \frac{\varepsilon_0}{2}\iiint |E(\boldsymbol{r};\omega)|^2 \mathrm{d}^3\boldsymbol{r} + \frac{\mu_0}{2}\iiint |H(r;\omega)|^2 \mathrm{d}^3\boldsymbol{r}$, integrated over the meta-atom volume, and normalized it to the trivial case of a transparent particle (same geometry as that of the cuboid but with the refractive index of $n = 1$) with the total energy of w_0. As shown with the purple color, at the condition of the minimum scattering, the calculated energy within the particle is non-zero and is almost 20 times larger than that of the trivial case ($w_T/w_0 \approx 20$), which indicates the significant localization of energy distribution inside the meta-atom. It should be noted that, while the same phenomenon has been recently observed in a recent study conducted by Valero *et al.* [94] with a cylindrical meta-atom supporting HA [92], the stored electric energy within the cuboid meta-atom is approximately two times higher than that of its cylindrical counterpart. However, to the best of our knowledge, both of these geometries possess significant enhancement compared to the previous conventional anapoles [13–19] and make them

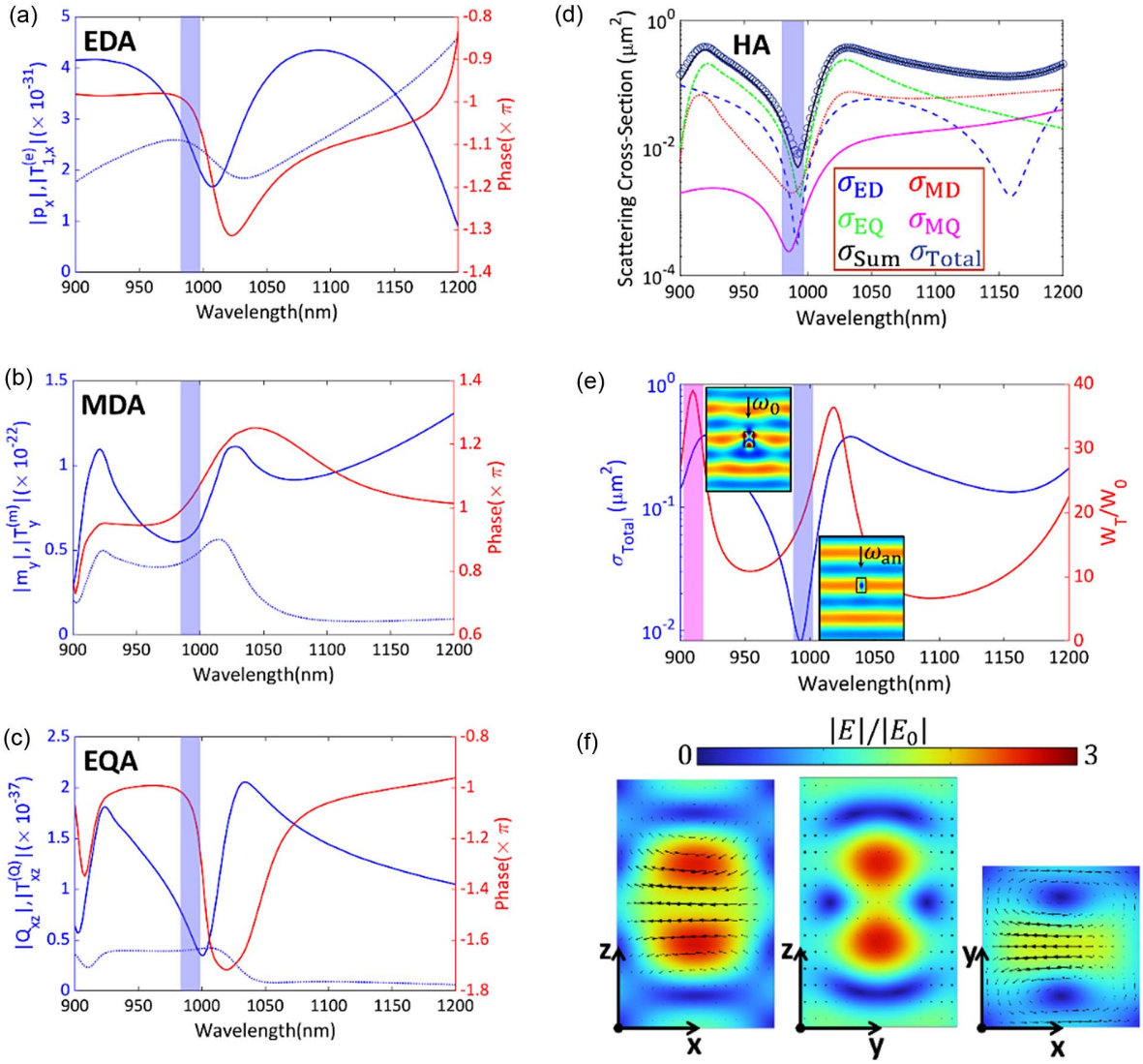

Fig. 4. Calculated amplitudes and phase differences between the primitive and toroidal contributions of a cuboid meta-atom with $W = 295$ nm and $H = 466$ nm for (a) ED, (b) MD, and (c) EQ scattering channels. In all plots, the amplitudes correspond to the left ordinate axis with a solid line representing primitive moments and dashed curves showing their toroidal counterparts, and the phase differences are read from the right ordinate axis. (d) Multipole decomposition of the cuboid meta-atom up to the magnetic quadrupole contribution. In the legend caption, "Sum" denotes the summation of the contributing moments up to the MQ term, while "Total" implies the total scattering cross-section calculated directly from COMSOL. (e) Calculated spectra corresponding to the radiated power (blue color) and stored electromagnetic energy normalized to the transparent particle (red color). The purple and magenta color bands denote the spectral positions corresponding to the dark and bright resonances, respectively, with their near-field profiles given in the insets. (f) Electric field distribution at the operating wavelength of 990 nm in three different planes of $z - x$, $z - y$, and $y - x$, with black arrows representing the displacement currents.

superior candidates for being used in scenarios wherein boosted light-matter interaction is required such as nonlinear enhancement of conversion efficiency [56–60]. We also note that, despite the existence of other higher energy peaks, such as the one highlighted with magenta color in Fig. 4(e), their corresponding scattering responses are not suppressed, making them visible to the outside observers, as shown in the inset. However, the simultaneous overlap of the corresponding zeros of the contributing moments leads to the low-scattering regime resulting in the meta-atom being "invisible," while the energy is stored inside of it, as shown in the inset of Fig. 4(e).

The quality factor (Q-factor) serves as a vital metric to gauge light-matter interaction strength. To determine the Q-factor of the presented scatterer, we implemented the quasi-normal mode (QNM) expansion framework [103,104]. In this perspective, the Q-factor of the dominant QNMs is calculated to be $Q = [28, 12, 39]$ with the mode lifetime of $\tau = [15, 6, 19]$ fs, which is higher than that of the traditional Mie-type resonances and can be a suitable alternative for material-intrinsic applications, such as nonlinear harmonic generation [58,105,106], nanolasers [107], and active metaphotonics at nanoscale [108,109]. Note that such simultaneous

energy storage and minimized scattering (non-radiative) regime occurred in the steady state, which is preceded by the transient period during which the energy is being accumulated in the cavity. It is also important to emphasize that the non-radiating anapole state, whether it is an EDA or HA, does not naturally arise as an eigenmode of the scatterer [110]. In other words, the anapole state cannot sustain itself as a self-oscillating cavity mode satisfying boundary conditions independently of any incident field. Instead, it represents a resonant distribution of induced currents that can be excited through a well-designed interplay between the incident beam's topology and the scatterer's geometry in the steady state as long as the incident beam interacts with the meta-atom [110]. However, once the light beam has completely passed through the scatterer, the anapole field distribution, which cannot independently satisfy the boundary conditions on the scatterer's surface, begins to radiate and rapidly dissipates its stored energy over time [110–113]. As was mentioned earlier, while the majority of the previous studies in the field of non-radiating states were limited to the excitation of electric dipole anapoles, recently, improved suppression of radiation and higher energy confinement as compared to the EDAs have been demonstrated at the HA state excited within a cylindrical meta-atom [94]. Therefore, we have also compared the optical response of our proposed cuboid meta-atom with that of a cylindrical particle that supports first- and second-order EDAs (see Appendix F). As counterintuitive as it can appear, despite the significant difference between the volumes of the two meta-atoms ($V_{\text{cuboid}}/V_{\text{cylinder}} \approx 3$), the scattering intensity of the HA state is found to be suppressed more than 23 times compared to its first-order EDA counterpart, whereas its stored energy is almost three times higher. We also note that the HA state corresponds to the 48 times better suppression of radiation to the far-field than its higher-order electric dipole anapoles, while its stored energy exceeds 2.5 times of second-order EDAs. Figure 4(f) shows the distribution of the electric field within the cuboid meta-atom at the corresponding wavelength of the HA state in three different planes of $z-x$, $z-y$, and $y-x$. Contrary to the field distribution in the $y-x$ plane, which renders the well-known EDA field profile with a vortex-like distribution of the displacement current shown with black arrows, the internal distributions of the fields in $z-x$ and $z-y$ planes exhibit more complicated profiles that are attributed to the mixture of electric and magnetic multipole moments. As the final remark, we note that, contrary to the concept of dark mode in plasmonics, where a resonance with null net dipole moment cannot be excited by a planar incident wave due to symmetry reasons, the provided HA state can be efficiently excited by a plane wave (or Gaussian beam), simplifying the future experimental studies.

4. FROM NON-SCATTERING TO SUPER-SCATTERING

It has been previously shown that the optical response of a subwavelength particle strongly depends on its orientation with respect to the direction of illumination such that certain spectral features emerge or get suppressed [114]. Such spectral dependence stems from the changes in the components of multipolar moments and the variations in the coupling efficiency of a particular Mie resonant mode as a function of illumination direction. Therefore, tuning the illumination angle can be used as another degree of freedom for controlling the spectral position of the higher-order anapoles in the spectral window of interest. Here we investigate how higher-order anapoles change as a function of illumination angle. First, we fixed the dimensions of the cuboid particle to be $W = 295$ nm and $H = 466$ nm and swept the illumination angle θ from 0° to 90° over the wavelength range of 900 nm $< \lambda <$ 1200 nm as it is schematically demonstrated in the inset of Fig. 5.

Figure 5(a) shows the total scattering cross-section of the cuboid meta-atom, which exhibits a symmetric response with respect to the angle of incidence due to the symmetric topology of the scatterer in the plane of incidence. Depending on the illumination direction, resonant peaks emerge or get suppressed leading to the formation of a region where the radiation to the far-field is strongly suppressed (HA state). As opposed to the conventional EDAs, the excitation of such a non-radiating state is possible in a wide range of incident angles from $-30° < \theta < 30°$ (rather than only at $\theta = 0°$) as shown with purple dashed line in Fig. 5(a). The multipole decomposition results shown in Figs. 5(b) and 5(c) show that tuning the angle of incidence yields the excitation/suppression of new resonances. In particular, several dips in the scattering spectra of the meta-atom are observed under oblique incidences, which are attributed to the destructive interference between the primitive and toroidal moments of the contributing Mie resonances as long as they are overlapping with the black dashed lines that are representing the regions wherein the phase difference conditions for inducing anapole states ($\varphi_P - \varphi_T \approx \pm\pi$) are satisfied. Taking the electric dipole response as an example, we note that only three lines coexist with the emerged resonant dips, indicating that, for these particular branches, both the amplitude and phase conditions are satisfied, and the EDA can be obtained and tuned with respect to the incident angle. For the magnetic dipole and electric quadrupole anapoles, such behavior becomes more complicated, and the anapole conditions are satisfied in the two regions shown in these plots. Interestingly, the higher-order anapole states can also be obtained at $\theta = 90°$, making them suitable platforms for on-chip applications. Figure 5(e) shows the optical response of the meta-atom corresponding to the incident angle changes from frontal ($\theta = 0°$) to lateral ($\theta = 90°$) illumination in the steps of 30°. While the overall scattering response of the scatterer changes significantly once the illumination angle varies, the optical behavior of the meta-atom at the operating wavelength of $\lambda = 990$ nm gradually transitions from a non-radiating hybrid anapole state (for $\theta = 0°$) to a radiative mode corresponding to a magnetic quadrupole (for $\theta = 90°$), as shown with the blue dashed curve. On the other hand, the scattering response of the same meta-atom can be tuned at $\lambda = 850$ nm from the radiative to the non-radiative state upon the continuous change of the illumination angle from $\theta = 0°$ to $\theta = 90°$, respectively. We note that the observed optical phenomena are not related to the common shifts in the scattering spectra studied previously [29] and result from the change in the coupling efficiency of light to a particular Mie-type resonant mode once the direction of illumination

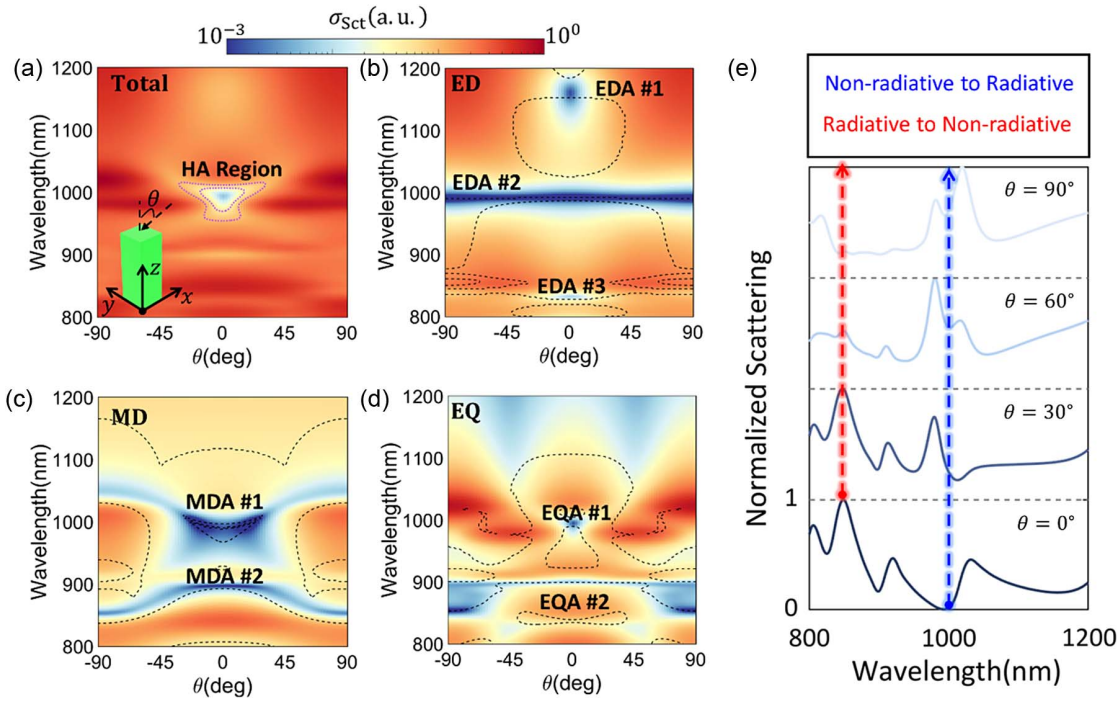

Fig. 5. (a) Normalized total scattering cross-section of the cuboid meta-atom under plane wave incidence with the angles θ ranging from 0° to 90° as functions of the operating wavelength. The calculated multipole decomposition results for (b) ED, (c) MD, and (d) EQ, with the dashed lines representing the regions wherein $\varphi_P - \varphi_T = \pm\pi$. Anapoles of any kind occur at the points where the dashed lines overlap with the scattering minima. (e) Total scattering cross-section for four different values of the incident angles $\theta = [0°, 30°, 60°, 90°]$ as functions of wavelength. Tuning the angle of incidence results in the changes in the meta-atom's response from non-radiative to radiative (blue line) and vice versa (red line) at two distinct wavelengths.

is changed. It should be remarked that, unless only one multipole determines the light scattering, the value and accuracy of moments depend on the choice of the origin of the coordinate system and the position where the multipoles are assumed to be located. As shown previously [99–102], for arbitrary shaped particles, it is convenient to choose the origin of coordinate as the center mass of the scatterer. However, when the meta-atom in question consists of a cluster of scatterers, the system center of mass does not necessarily coincide with the origin of the coordinate, and the moments are assumed to be shifted with respect to the origin [115–117]. Recently, the pioneering work proposed by Ospanova *et al.* [118] has shown that the shift in the multipoles leads to the change of the conventional moments and emergence of new terms. However, in the case of plane wave oblique incidence, the center mass of the scatterer does not shift since the geometrical features remain unchanged, and as a result, the expressions for describing moments still hold true. In particular, such a problem (i.e., isolated scatterer under oblique incidence) has been extensively studied before [32,119–121], and it has been shown both numerically and experimentally that the optical response of the meta-atom in question can be correctly described by the unmodified expressions.

So far, we have discussed the excitation of an HA state within a cuboid meta-atom possessing inversion symmetry along the z axis. In particular, the inversion symmetry of the optical scatterer results in the eigenmodes consisting of either only even (MD, EQ, etc.) or only odd (ED, MQ, etc.) multipoles, which can constructively/destructively interfere with one another as schematically shown in Fig. 6(a). However, as it has been recently shown by Poleva *et al.* [122], breaking the inversion symmetry of the particle can lead to bianisotropic responses such that the ED and MD are mutually coupled, and the corresponding eigenmodes of the meta-atom become a combination of multipoles with mixed parities [see Fig. 6(b)], leading to the improvement of the directivity of a particular eigenmode [97]. Here, we demonstrate that, by breaking the inversion symmetry of the meta-atom from a cuboid to a pyramid geometry, the scattering response can be changed from a non-scattering hybrid anapole state (for cuboid geometry) to a super-scattering regime (pyramid structure) as a result of the transition from non-bianisotropic to bianisotropic optical responses. In particular, each multipole in the scattering cross-section spectra represents an independent scattering channel that has an upper bound, known as the single-channel limit, which is bounded to $(2l+1)\lambda^2/2\pi$, wherein l represents the order of the multipole. Conventionally, the notation of super-scattering applies to the cases where the total scattering cross-section surpasses the given single-channel limit of an electric dipole ($l = 1$) such that $\frac{\sigma_{\text{Total}}}{\sigma_{\text{ED}}^{\max}} = \frac{2\pi\sigma_{\text{Total}}}{3\lambda^2} > 1$ [69–74]. To clarify how the transition of the topology of the meta-atom from non-bianisotropic to bianisotropic can lead to a super-scattering regime, we fixed the height of the scatterer to be the same as that of previous sections while the top-to-bottom

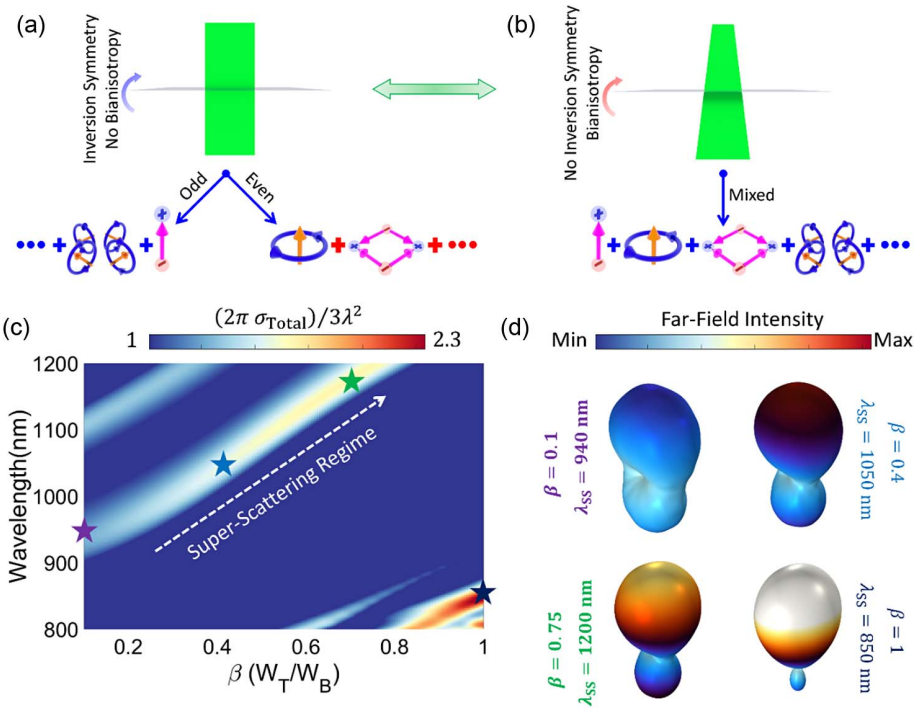

Fig. 6. Schematic demonstration of achieving bianisotropic responses via breaking the inversion symmetry of the meta-atom. For (a) symmetric particles, the eigenmodes consist of either only even or odd multipoles, while for (b) asymmetric meta-atoms, the optical response consists of multipoles of mixed parities. (c) Calculated response of the pyramid meta-atom with respect to the top-to-bottom width ratio and operating wavelength. Four various points corresponding to different values of $\beta = [0.1, 0.4, 0.75, 1]$ are indicated by stars and super-scattering regime occurs once $\frac{2\pi\sigma_{\text{Total}}}{3\lambda^2} > 1$. (d) Radiation pattern of the far-field intensity calculated at the wavelength corresponding to the super-scattering state for the meta-atoms with dimensions marked by stars in panel (c).

width ratio ($\beta = W_T/W_B$) is changed in the range of $0.1 < \beta = \frac{W_T}{W_B} < 1$ and calculated $\frac{2\pi\sigma_{\text{Total}}}{3\lambda^2}$ with respect to β and operating wavelength as shown in Fig. 6(c).

As can be seen from the calculated response, a strong super-scattering regime ($\frac{2\pi\sigma_{\text{Total}}}{3\lambda^2} \approx 2.3$) can be obtained for a near-perfect inversion symmetric meta-atom ($0.8 < \beta < 1$) in a narrow spectral range, whereas an asymmetric meta-atom ($\beta < 0.8$) can support super-scattering optical response in a broad spectral range of 900–1200 nm with lower amplitude of 1.6. Such an optical response is a result of breaking inversion symmetry, which not only leads to a bianisotropic response but also achieves super-scattering behavior that exceeds the single-channel limit by a factor of 2.3. The contributions of each moment (up to MQ) are also calculated and provided in Appendix G. In Fig. 6(d), we demonstrate the far-field intensity of the meta-atom for $\beta = [0.1, 0.4, 0.75, 1]$ [marked by stars in Fig. 6(c)] at the operating wavelength corresponding to the maximum value of the super-scattering spectrum marked in Fig. 6(c). As can be seen from these radiation patterns, while for all the proposed cases directional scattering can be observed in the super-scattering regime, the magnitudes of the radiation patterns increase once the meta-atom geometry changes from asymmetric to inversion symmetric topology. Such a variation in the directivity of the meta-atoms is due to the spectral overlap of all the resonant modes for $\beta = 1$, whereas for other cases ($\beta = [0.1, 0.4, 0.7]$) fewer multipoles are overlapping with one another. These results demonstrate the role of inversion symmetry in realizing the super-scattering regime. Although recently it has been argued that the SCR of a scatterer with arbitrary size and shape does not have a maximum limit [123], the scattering limitations defined for spherical scatterers ($3\lambda^2/2\pi$) are remained in the literature as a benchmark for establishing super-scattering regime [69–74]. We note that the transition from the non-scattering to super-scattering states can be explained in the perspective of Fano-like profiles. Fano resonance typically emerges when a discrete quantum state interferes with a continuum of states. This interference can be described in the scattering spectrum, by the modified Fano formula as $\sigma = \sigma_{\text{bg}} + (\sigma_0/1+q^2) \times [(q+\Omega)^2/1+\Omega^2]$, wherein E represents the energy; $q = -\cot(\delta)$ is the Fano parameter; $\Omega = 2(E - E_0)/\Gamma$, with E_0 and Γ denoting the resonance energy and linewidth; and δ is the phase shift between the resonant mode and the background contribution coming from other modes and nonresonant scattering [124,125]. In particular, in the modified Fano formula, σ_0 denotes the smooth peak envelope and σ_{bg} represents the background contribution of the scatterer's nonresonant modes. While it has been shown that the spectrum of Mie scattering can be presented in the form of an infinite series of the Fano profiles [126], here we just limit ourselves to the spectral regions wherein the desired optical response, being non-scattering or super-scattering, is presented. In the context of the HA within 960 nm $< \lambda <$ 1040 nm (corresponding to 1.19 eV $< E <$ 1.29 eV) and under normal incidence, the optical response

exhibits Fano-like asymmetric behavior, with the Fano parameter of $q = -0.95$ representing minimized radiative losses due to the interference between primitive and toroidal contributions. The formation of the super-scattering state can similarly be described via the Fano profile. In particular, by varying β from 0.1 to 1, the Fano parameter changes from −1.97 to 1.49, leading to different scattering profiles, with the alternation of scattering enhancement compared to the single channel limit (at their corresponding wavelengths) from 1.26 to 2.3. Interestingly, the provided results indicate that breaking the out-of-plane symmetry allows for on-demand tuning of the asymmetry factor (q), yielding the manipulation of the meta-atom's quality factor and field confinement at nanoscale. We also note that the same optical phenomenon can be observed under different angles of illuminations as shown in Fig. 5. In particular, once the incident angle deviates from $\theta = 0°$, the non-radiating state tends to be radiative, which manifests itself in the change of the Fano parameter value and, consequently, the scattering spectrum. Such a change in the Fano parameter value is a manifestation of variation in the phase shift (δ) between the dominant resonant mode and the background contribution coming from other modes. As a final remark, we note that, while the exploration of hybrid anapoles has been pursued before, our paper uniquely navigates two contrasting regimes of light-matter interaction on a unified platform. We unravel the intricacies of transitioning from non-scattering to super-scattering and the pivotal role illumination angles play in achieving specific radiative features. Our findings dive deep into the dynamics of various anapole types, shedding light on how geometry and symmetry intricately shape the optical response and energy confinement within a meta-atom.

5. CONCLUSION

As opposed to the conventional EDAs, in this work, we predicted and demonstrated new non-radiative states supported by cuboid meta-atoms, formed due to the destructive interference between electric and magnetic primitive and toroidal contributions. In particular, we theoretically predicted and numerically showed that a cuboid meta-atom can support higher-order non-radiative states up to the electric quadrupole moment at the same operating wavelength, leading to significant suppression of the far-field radiation and a remarkable 20-fold enhancement of energy stored inside the subwavelength dielectric particle. We also explored the role of the illumination angle in the optical response of such a non-scattering state and demonstrated that, depending on the orientation of the meta-atom, its scattering response switches from non-radiating to radiating states. Moreover, we revealed that tuning the topology of the meta-atom from a symmetric to an asymmetric one leads to the super-scattering state, which is an opposite regime of light-matter interaction as compared to its non-scattering counterpart, with 130% enhancement in its scattering behavior. The discovered concept of the hybrid anapole state as well as the anapole to super-scattering transition is likely to enable a plethora of potential applications ranging from remote sensing relying on the shape and orientation of meta-atoms to the enhancement of nonlinear conversion efficiency and establishing strong coupling between photonic and excitonic platforms.

APPENDIX A: MULTIPOLE DECOMPOSITION

Recently, several theoretical frameworks, which are based on the irreducibility of Cartesian tensors with respect to the SO(3) group, have been proposed to unambiguously describe the toroidal contributions in the scattering spectra of optical scatterers [93]. According to the theory of irreducible multipoles, the dyadic-like form of the scattered field in the far-field region up to magnetic quadrupole can be expressed as

$$\begin{aligned}
&\boldsymbol{E}_{\mathrm{Sct}}(\boldsymbol{n},\omega)\\
&= \frac{k_0^2\,\exp(ik_0 r)}{4\pi\epsilon_0 r}\Bigg(\Bigg(\boldsymbol{n}\times\Bigg(\Bigg(\boldsymbol{p}(\omega)+\frac{ik_0\epsilon_d}{c}\boldsymbol{T}_1^{(e)}(\omega)\\
&\quad+\frac{ik_0^3\epsilon_d^2}{c}\boldsymbol{T}_2^{(e)}(\omega)\Bigg)\times\boldsymbol{n}\Bigg)\Bigg)\\
&\quad+\frac{1}{c}\Bigg(\Bigg(\boldsymbol{m}(\omega)+\frac{ik_0\epsilon_d}{c}\boldsymbol{T}^{(m)}(\omega)\Bigg)\times\boldsymbol{n}\Bigg)\\
&\quad+\frac{ik_0}{2c}\Bigg(\boldsymbol{n}\times\Bigg(\boldsymbol{n}\times\Bigg(\Bigg(\hat{Q}^{(m)}(\omega)+\frac{ik_0\epsilon_d}{c}\hat{T}^{(Q_m)}(\omega)\Bigg)\cdot\boldsymbol{n}\Bigg)\Bigg)\Bigg)\\
&\quad+\frac{ik_0}{2c}\boldsymbol{n}\Bigg(\Bigg(\hat{Q}^{(m)}(\omega)+\frac{ik_0\epsilon_d}{c}\hat{T}^{(Q_m)}(\omega)\Bigg)\cdot\boldsymbol{n}\Bigg)\Bigg)\Bigg), \qquad \textbf{(A1)}
\end{aligned}$$

where $\boldsymbol{n} = \boldsymbol{r}/r$ is the unit vector directed from the particle's center toward an observation point. Using these notations, the far-field scattered power can be readily related to the scattered fields of Eq. (A1) with the aid of a time-averaged Poynting vector as $\mathrm{d}P_{\mathrm{Sct}} = 0.5\sqrt{\epsilon_0/\mu_0}|\boldsymbol{E}_{\mathrm{Sct}}|^2 r^2 \mathrm{d}\Omega$, wherein $\mathrm{d}\Omega = \sin\theta \mathrm{d}\theta\mathrm{d}\varphi$ represents the solid angle [101]. Therefore, combining Eq. (A1) with the given relation of scattered power and performing the integration over the total solid angle, the scattering cross-section, defined as $\sigma_{\mathrm{Sct}} = 2\sqrt{\mu_0/\epsilon_0\epsilon_d}\cdot\left(\frac{P_{\mathrm{Sct}}}{|\boldsymbol{E}_{\mathrm{inc}}|^2}\right)$, with $\boldsymbol{E}_{\mathrm{inc}}$ representing the incident wave, can be obtained as that of Eq. (1).

APPENDIX B: ELECTRIC TOROIDAL DIPOLES OF THE FIRST AND SECOND KINDS

The destructive interference between the first and second types of electric toroidal dipole moments $[\boldsymbol{T}_1^{(e)}(\omega) + ik_0^2\epsilon_d\boldsymbol{T}_2^{(e)}(\omega) = 0]$ can also lead to the toroidal anapole state. However, on account of the negligible strength of $\boldsymbol{T}_2^{(e)}(\omega)$, compared to its first-type counterpart, the observation of such a non-radiating state has remained within the theoretical framework, and to the best of our knowledge, it has not been shown numerically or experimentally so far. Figure 7 demonstrates the optical response of the electric dipole moment as a function of the operating wavelength, wherein the amplitude and phase differences between the electric dipole and its first- and second-type toroidal counterparts are shown with blue and red colors, respectively.

As can be seen from this figure, the amplitude of the second-type electric toroidal moment (shown with blue circles) is one order of magnitude lower than that of its first type in a broad spectral window of interest. However, at the shorter wavelength, the amplitude of the toroidal contributions becomes comparable, providing an opportunity to achieve a toroidal anapole

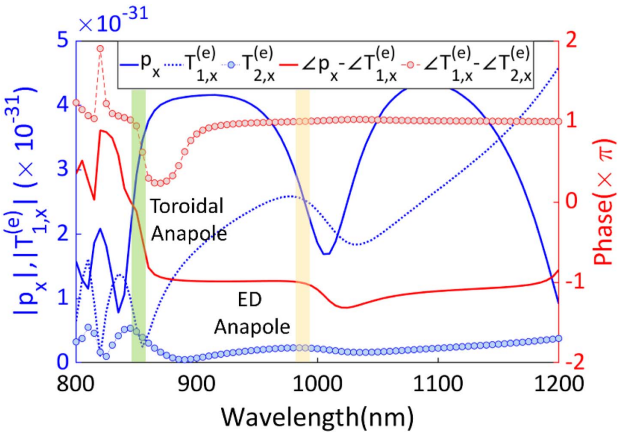

Fig. 7. Calculated amplitudes and phase differences between the electric primitive and first- and second-type toroidal multipoles of a cuboid meta-atom with $W = 295$ nm and $H = 466$ nm. The amplitudes correspond to the left ordinate axis with a solid line representing the primitive moment, a dashed curve denoting the first type of electric toroidal moment, and a circle graph showing the second type of toroidal moment, and the phase differences are read from the right ordinate axis.

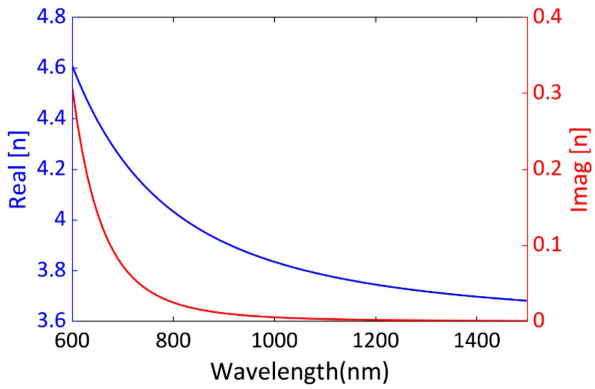

Fig. 8. Real (blue line) and imaginary (red curve) parts of polysilicon refractive index.

once its corresponding condition is satisfied [i.e., $|\boldsymbol{T}_1^{(e)}(\omega)| \approx |ik_0^2\epsilon_d \boldsymbol{T}_2^{(e)}(\omega)|$ and $\angle\boldsymbol{T}_1^{(e)}(\omega) - \angle ik_0^2\epsilon_d \boldsymbol{T}_2^{(e)}(\omega) \approx \pm\pi$]. In particular, such a criterion is fulfilled at the spectral position of $\lambda = 850$ nm, as highlighted with a green bar in Fig. 7, indicating the excitation of the toroidal electric dipole anapole (TEDA) state. Nevertheless, owing to the presence of a strong primitive electric dipole at this operating wavelength, the optical response of the meta-atom is mainly governed by the ED contribution, and the TEDA effect will be hidden.

APPENDIX C: NUMERICAL SIMULATIONS

The numerical simulations have been carried out using the finite-element method (FEM) implemented in the commercial software COMSOL Multiphysics. In particular, we utilized the Wave Optics Module to solve Maxwell's equations in the frequency domain together with proper boundary conditions. We used a spherical domain filled with air and having a radius of 4λ as the background medium, while perfectly matched layers of thickness 0.6λ were positioned outside of the background medium to act as absorbers and avoid undesired scattering. The tetrahedral mesh was also chosen to ensure the accuracy of the results and allow numerical convergence. As we have recently shown in Ref. [114], although the type of illumination beam can significantly affect the excited multipolar moments, the key point in the evaluation of scattering cross-section is the calculation of the induced displacement currents within the resonator and then associating the multipolar moments according to the given expressions of Eqs. (2) and (3). Since in this paper we are mainly interested in the effect of meta-atom topology in inducing two opposite regimes of light-matter interactions (i.e., HA and super-scattering), we have limited our study to the case of plane wave illumination (electric field polarized along the x axis), yet the interaction of other light beams, known as structured lights, is expected to provide exotic optical responses, which will be discussed elsewhere. We also note that the polysilicon refractive index was taken from ellipsometry measurements, and its results are provided in Fig. 8.

APPENDIX D: OPTICAL DYNAMICS OF MAGNETIC QUADRUPOLE

To investigate the effect of meta-atom geometry on the magnetic quadrupole moment, we follow the same procedure outlined earlier. In the first case, we fix the meta-atom width to $W = 295$ nm and change its height from 300 to 500 nm, while in the second scenario, the height is set to $H = 466$ nm, and the width is changed from 100 to 310 nm over the wavelength range of 850–1150 nm. The dynamics of the MQ moment are studied by integrating the displacement current induced within the meta-atom using Eqs. (2) and (3) of the main manuscript, as shown in Fig. 9(a) and 9(b), respectively.

As seen from Figs. 9(a) and 9(b), changing the height of the meta-atom has a negligible effect on the scattering cross-section of the MQ channel, whereas the variation of scatterer width can significantly shift the emerged dip within the MQ spectrum. We note that, despite the excitation of three higher-order anapoles at the operating wavelength of $\lambda_o = 990$ nm, the MQA conditions are not satisfied within this region, as demonstrated in Figs. 9(c) and 9(d) for the amplitude and phase difference, respectively. In particular, although the amplitude condition is satisfied for $\lambda_o = 990$ nm [see Fig. 9(a)], the phase condition is not fulfilled, and its value corresponds to $\angle\hat{Q}_{yz}^{(m)} - \angle\hat{T}_{yz}^{(Q_m)} \approx 0.13\pi$. Therefore, the non-radiating optical response of the meta-atom at this particular spectral position is merely attributed to the EDA, MDA, and EQA. Nevertheless, as can be seen from Figs. 9(c) and 9(d), for $H < 450$ nm and at shorter wavelengths, the MQA can be excited within the scatterer.

APPENDIX E: EXPLICIT CONTRIBUTIONS OF PRIMITIVE AND TOROIDAL MOMENTS AS FUNCTIONS OF WIDTH

To study the effect of width on the optical response of the cuboid meta-atom and clarify the origins of the emerged dips within the scattering spectra shown in Fig. 2, we evaluate

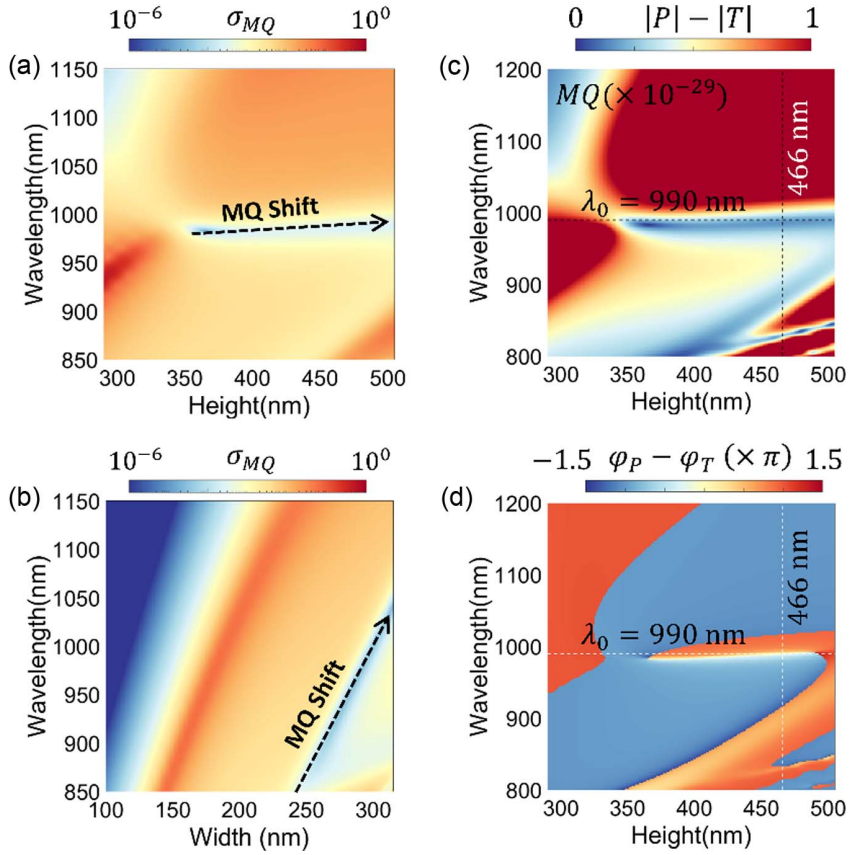

Fig. 9. Contribution of MQ moment excited within the cuboid scatterer as a function of (a) height and (b) width with respect to wavelength. Changing the height of the meta-atom has a negligible effect on the MQ response, while the variation of its width can significantly shift the scattering response. (c), (d) Contributions of both primitive and toroidal MQ multipole moments as functions of height and wavelength. At the spectral position wherein the optical response of the meta-atom is mainly governed by higher-order anapole states up to EQA (shown with black dashed lines), the conditions for satisfying magnetic quadrupole anapole are not fulfilled.

the explicit dynamics of both primitive and toroidal contributions as functions of width (100 nm $< W <$ 300 nm) over the wavelength range of 900–1200 nm and identify the regions wherein the conditions of inducing anapoles $|P| - |T| \approx 0$ and $\varphi_P - \varphi_T \approx \pm\pi$ are satisfied with respect to the operating wavelength as shown in Fig. 10.

As can be seen from these figures, while three branches of resonant dips emerge within the amplitude spectra of the ED multipole, the phase difference condition ($\varphi_{p_x} - \varphi_{T_x} \approx \pm\pi$) is merely fulfilled in two branches, leading to the excitation of electric dipole anapoles. On the other hand, by changing the width of the meta-atom, typically for 200 nm $< W <$ 295 nm, the magnetic dipole anapole can be obtained in a broader spectral range of 900–1000 nm. Interestingly, the EQA response is significantly altered by changing the meta-atom width, and both the amplitude and phase conditions are satisfied in a broad spectral range.

APPENDIX F: OPTICAL RESPONSE OF HYBRID ANAPOLE COMPARED TO CONVENTIONAL EDA

Here, we compare the optical response of a cylindrical meta-atom supporting higher-order anapole (HAOM) states [127] with that of a cuboid scatterer hosting a hybrid anapole. For this purpose, we implement a polysilicon cylindrical meta-atom with a diameter of D and diameter-to-height aspect ratio of $\alpha = D/H$, and we evaluate its optical response as a function of D, α, and operating wavelength as shown in Fig. 11. As seen from Fig. 11(a), tuning the aspect ratio leads the overall scattering response of the meta-atom to vary such that HAOM up to the fourth order emerges within the scattering spectra. To further clarify the origin of the emerged dips in the scattering spectra, we employed the Cartesian multipole decomposition for the case of $D = 610$ nm and $H = 50$ nm and also calculate its total stored energy with respect to the operating wavelength, as shown in Figs. 11(b) and 11(c), respectively. As can be seen from Fig. 11(b), we note that, the same as that of their fundamental counterparts, the electric dipole moments at the wavelength corresponding to the excitation of HAOM possess minimal values with maximal energy confinement, as verified numerically in Fig. 11(c). We also calculate the optical response of the cylindrical meta-atom for a fixed aspect ratio of $\alpha = 10$ as a function of diameter and operating wavelength in Fig. 11(c). As can be seen from these results, by decreasing the diameter of the scatterer from 1200 to 600 nm, its optical response blue-shifts toward shorter wavelengths, thus providing an opportunity to spectrally overlap the desired electric anapole (1st, 2nd, 3rd, etc.) at the same wavelength as that of the HA state as

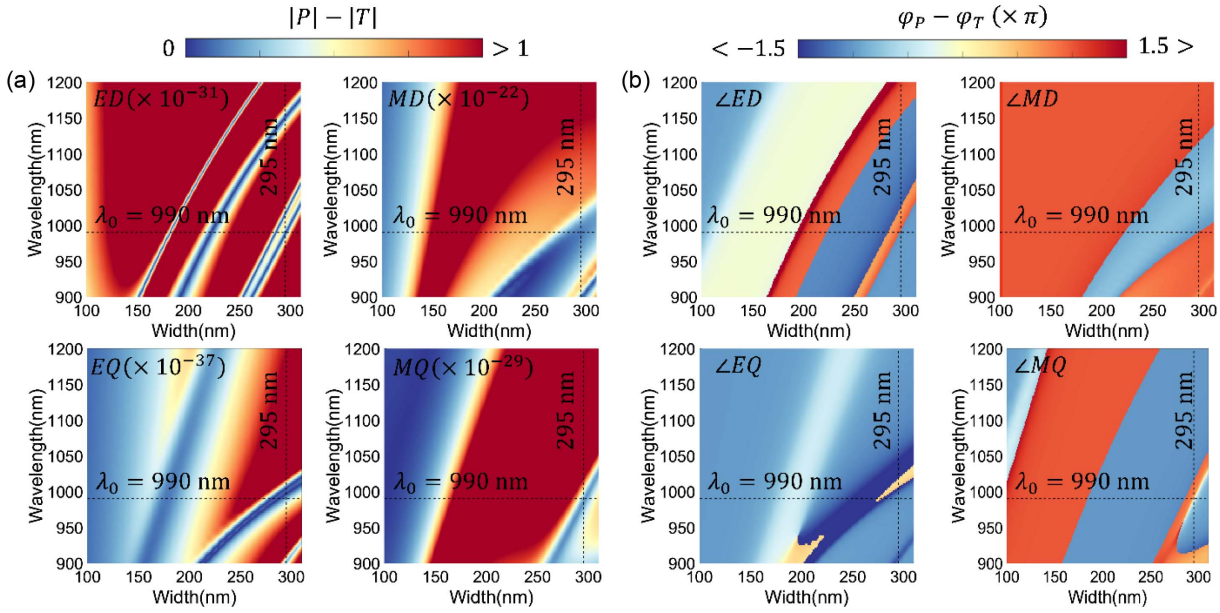

Fig. 10. Explicit dynamics of (a) amplitude and (b) phase of primitive and toroidal contributions as functions of height and wavelength for ED, MD, EQ, and MQ. An anapole of any kind is excited in regions wherein both conditions are simultaneously satisfied. The vertical dashed line corresponds to the dimension at which the HA state can be excited up to the EQA at the operating wavelength of $\lambda = 990$ nm (horizontal dashed line).

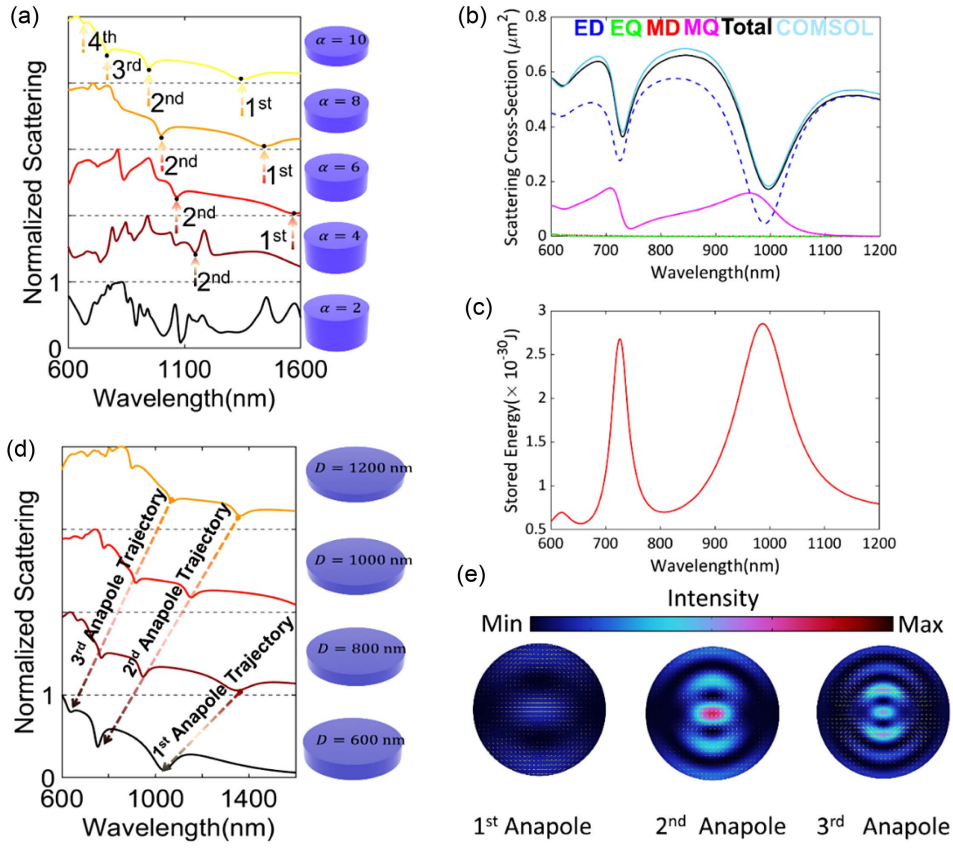

Fig. 11. (a) Evolution of the scattering cross-section under the continuous change of the diameter-to-height aspect ratio. (b) Multipole decomposition and (c) stored energy spectra for a cylindrical particle with $D = 605$ nm and $H = 50$ nm. (d) Optical response of the cylindrical metaatom as a function of diameter and wavelength. By changing the diameter, the spectral position of the desired electric dipole anapole can be tuned. (e) The near-field distribution of first-, second-, and third-order electric anapole states at their corresponding excited wavelengths.

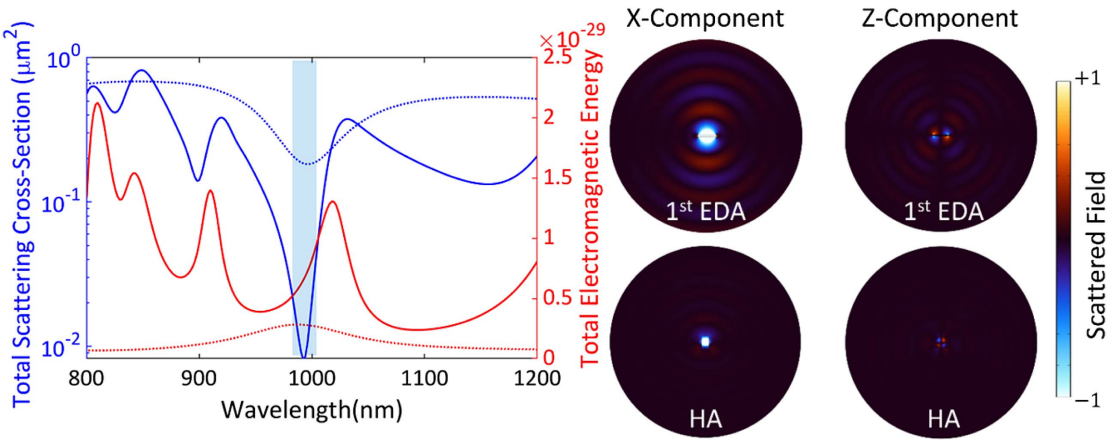

Fig. 12. Calculated total scattering cross-section (blue color) and stored energy (red color) of two meta-atoms supporting HA (solid line) and first-order EDA (dashed curve) as a function of the operating wavelength. The scattered field's x and z components at the corresponding wavelength of anapole excitation are also given as a point of comparison.

was shown in the main manuscript. To verify the existence of HAOM within the proposed meta-atom, we have also calculated electric field distribution within the cylindrical meta-atom, and its results are collated in Fig. 11(d). As can be seen from this panel, at the spectral position wherein the far-field scatterings are minimum (i.e., higher-order electric anapole states are excited), the near-field distribution possesses vortex-like behavior with $2N+1$ lobes (N represents the order of the anapole), which agrees well with the results proposed recently in Ref. [105].

Followed by the provided results of Fig. 11 and the evolution of the optical response of the scatterer as a function of its

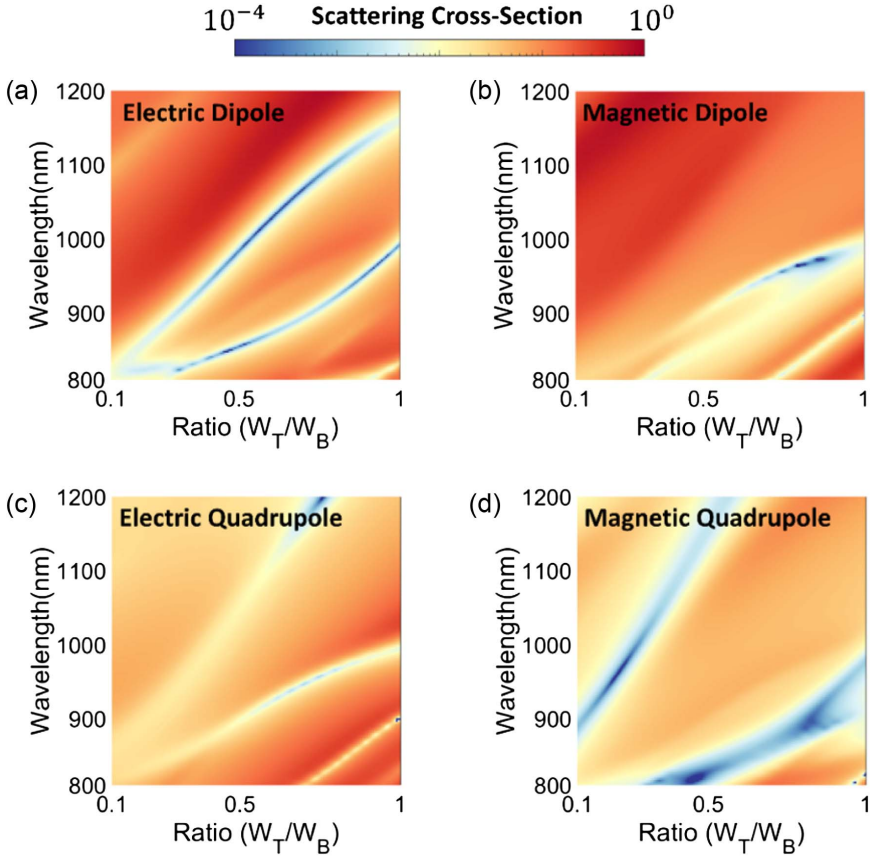

Fig. 13. Calculated scattering cross-sections of the cuboid meta-atom for (a) ED, (b) MD, (c) EQ, and (d) MQ multipole moments as functions of β and the operating wavelength. The asymmetric parameter corresponding to the inversion symmetry can be used as another degree of freedom to manipulate the emerged resonant dips within the scattering spectra.

dimension, we set the diameter and aspect ratio of the cylindrical meta-atom to be $D = 605$ nm and $\alpha = 12.1$, respectively, calculating its total scattering cross-section as well as its total energy and comparing it with the case of HA as it is shown in Fig. 12. As can be seen from this figure, the total scattering cross-section of the 1st EDA, shown with a dashed blue curve, is 23 times higher than that of the HA (solid blue line), while its stored energy (dashed red curve) is almost threefold lower than its HA counterpart. As a result of such a significant contrast between the maximal value of radiation suppression, it is expected that the first-order EDA will possess radiative behavior compared to HA as it is also numerically verified by evaluating their scattered fields at $\lambda_0 = 990$ nm.

As a final remark, according to the results provided in Fig. 11, the spectral position of the HAOM can also be tuned to overlap with HA. However, as this required tedious numerical calculations and was not in the scope of this paper, we have disregarded such a spectral overlap and, in turn, directly compared the stored energy as well as the radiation suppression of HAOM (at their corresponding wavelengths) with that of HA and noticed that the HA could suppress the radiation to the far-field more than 48 times better than higher-order electric dipole anapoles, while its stored energy exceeds 2.5 times of higher-order EDAs.

APPENDIX G: CALCULATED MULTIPOLE MOMENTS AS FUNCTIONS OF TOP-TO-BOTTOM RATIO

As shown in the main manuscript, breaking the scatterer's out-of-plane inversion symmetry makes changing its optical response from a non-scattering to a super-scattering state possible. Here, we demonstrate how the excited multipole moments within the scatterer are altered as a function of the top-to-bottom width ratio (β) and operating wavelength as shown in Fig. 13.

As can be seen from these figures, we conclude that, once the out-of-plane inversion symmetry is broken ($\beta \neq 1$), the scattering response of the excited moments within the cuboid meta-atom varies significantly, yielding the emergence and suppression of new resonances for various values. Such a variation in the optical response of the subwavelength scatterer suggests that the asymmetric parameter can be used as another degree of freedom for the scattering manipulation at the nanoscale. In particular, for $0.1 < \beta < 0.5$, the strong magnetic quadrupole anapole state emerges within the scatterer's optical spectra, shifting toward a longer wavelength as the asymmetric parameter increases.

Funding. Army Research Office (W911NF1810348); National Science Foundation (1809518); Office of Naval Research (N00014-20-1-2558).

Disclosures. The authors declare no conflicts of interest.

Data Availability. The data that support the findings of this study are available from the corresponding author upon reasonable request.

REFERENCES

1. D. J. Griffiths and D. F. Schroeter, *Introduction to Quantum Mechanics* (Cambridge University, 2018).
2. N. Zettili, "Chapter 1: Origins of quantum physics," in *Quantum Mechanics: Concepts and Applications* (Wiley, 2009), pp. 31–36.
3. R. Shankar, *Principles of Quantum Mechanics* (Springer, 2012).
4. I. B. Zel'Dovich, "Electromagnetic interaction with parity violation," Sov. Phys. JETP **6**, 1184–1186 (1958).
5. C. S. Wood, S. C. Bennett, D. Cho, *et al.*, "Measurement of parity nonconservation and an anapole moment in cesium," Science **275**, 1759–1763 (1997).
6. E. E. Radescu, "On the electromagnetic properties of Majorana fermions," Phys. Rev. D **32**, 1266–1268 (1985).
7. C. M. Ho and R. J. Scherrer, "Anapole dark matter," Phys. Lett. B **722**, 341–346 (2013).
8. Y. Gao, C. M. Ho, and R. J. Scherrer, "Anapole dark matter at the LHC," Phys. Rev. D **89**, 045006 (2014).
9. V. V. Flambaum and I. B. Khriplovich, "P-odd nuclear forces: a source of parity violation in atoms," Sov. Phys. JETP **52**, 835–839 (1980).
10. V. V. Flambaum, I. B. Khriplovich, and O. P. Sushkov, "Nuclear anapole moments," Phys. Lett. B **146**, 367–369 (1984).
11. W. C. Haxton, E. M. Henley, and M. J. Musolf, "Nucleon and nuclear anapole moments," Phys. Rev. Lett. **63**, 949–952 (1989).
12. V. M. Dubovik and A. A. Cheshkov, "Form-factors and multipoles in electromagnetic interactions," Sov. Phys. JETP **24**, 924–926 (1965).
13. V. A. Fedotov, A. V. Rogacheva, V. Savinov, *et al.*, "Resonant transparency and non-trivial non-radiating excitations in toroidal metamaterials," Sci. Rep. **3**, 2967 (2013).
14. A. E. Miroshnichenko, A. B. Evlyukhin, Y. F. Yu, *et al.*, "Nonradiating anapole modes in dielectric nanoparticles," Nat. Commun. **6**, 8069 (2015).
15. V. Savinov, N. Papasimakis, D. P. Tsai, *et al.*, "Optical anapoles," Commun. Phys. **2**, 69 (2019).
16. K. V. Baryshnikova, D. A. Smirnova, B. S. Luk'yanchuk, and Y. S. Kivshar, "Optical anapoles: concepts and applications," Adv. Opt. Mater. **7**, 1801350 (2019).
17. P. C. Wu, C. Y. Liao, V. Savinov, *et al.*, "Optical anapole metamaterial," ACS Nano **12**, 1920–1927 (2018).
18. Y. Yang and S. I. Bozhevolnyi, "Nonradiating anapole states in nanophotonics: from fundamentals to applications," Nanotechnology **30**, 204001 (2019).
19. R. M. Saadabad, L. Huang, A. B. Evlyukhin, *et al.*, "Multifaceted anapole: from physics to applications," Opt. Mater. Express **12**, 1817–1837 (2022).
20. H.-T. Chen, A. J. Taylor, and N. Yu, "A review of metasurfaces: physics and applications," Rep. Prog. Phys. **79**, 076401 (2016).
21. F. Ding, A. Pors, and S. I. Bozhevolnyi, "Gradient metasurfaces: a review of fundamentals and applications," Rep. Prog. Phys. **81**, 026401 (2017).
22. C.-W. Qiu, T. Zhang, G. Hu, *et al.*, "Quo vadis, metasurfaces?" Nano Lett. **21**, 5461–5474 (2021).
23. A. M. Shaltout, V. M. Shalaev, and M. L. Brongersma, "Spatiotemporal light control with active metasurfaces," Science **364**, eaat3100 (2019).
24. C. Gigli, Q. Li, P. Chavel, *et al.*, "Fundamental limitations of Huygens' metasurfaces for optical beam shaping," Laser Photonics Rev. **15**, 2000448 (2021).
25. W. T. Chen, A. Y. Zhu, and F. Capasso, "Flat optics with dispersion-engineered metasurfaces," Nat. Rev. Mater. **5**, 604–620 (2020).
26. N. Yu and F. Capasso, "Flat optics with designer metasurfaces," Nat. Mater. **13**, 139–150 (2014).
27. W. Liu and Y. S. Kivshar, "Generalized Kerker effects in nanophotonics and meta-optics," Opt. Express **26**, 13085–13105 (2018).
28. Y. Kivshar and A. Miroshnichenko, "Meta-optics with Mie resonances," Opt. Photonics News **28**, 24–31 (2017).
29. T. Liu, R. Xu, P. Yu, *et al.*, "Multipole and multimode engineering in Mie resonance-based metastructures," Nanophotonics **9**, 1115–1137 (2020).

30. H. K. Shamkhi, K. V. Baryshnikova, A. Sayanskiy, *et al.*, "Transverse scattering and generalized Kerker effects in all-dielectric Mie-resonant metaoptics," Phys. Rev. Lett. **122**, 193905 (2019).
31. H. K. Shamkhi, A. Sayanskiy, A. C. Valero, *et al.*, "Transparency and perfect absorption of all-dielectric resonant metasurfaces governed by the transverse Kerker effect," Phys. Rev. Mater. **3**, 085201 (2019).
32. X. Zhang and A. L. Bradley, "Wide-angle invisible dielectric metasurface driven by transverse Kerker scattering," Phys. Rev. B **103**, 195419 (2021).
33. C. Li, X. Ouyang, J. Sun, *et al.*, "Transverse scattering from nanodimers tunable with generalized cylindrical vector beams," Laser Photonics Rev. **17**, 2200867 (2023).
34. V. E. Babicheva and A. B. Evlyukhin, "Resonant lattice Kerker effect in metasurfaces with electric and magnetic optical responses," Laser Photonics Rev. **11**, 1700132 (2017).
35. V. E. Babicheva, "Lattice effect in Mie-resonant dielectric nanoparticle array under oblique light incidence," MRS Commun. **8**, 1455–1462 (2018).
36. A. V. Prokhorov, P. D. Terekhov, M. Y. Gubin, *et al.*, "Resonant light trapping via lattice-induced multipole coupling in symmetrical metasurfaces," ACS Photonics **9**, 3869–3875 (2022).
37. P. C. Wu, R. A. Pala, G. K. Shirmanesh, *et al.*, "Dynamic beam steering with all-dielectric electro-optic III–V multiple-quantum-well metasurfaces," Nat. Commun. **10**, 3654 (2019).
38. P. Berini, "Optical beam steering using tunable metasurfaces," ACS Photonics **9**, 2204–2218 (2022).
39. J. Yang, S. Gurung, S. Bej, *et al.*, "Active optical metasurfaces: comprehensive review on physics, mechanisms, and prospective applications," Rep. Prog. Phys. **85**, 036101 (2022).
40. L. Huang, S. Zhang, and T. Zentgraf, "Metasurface holography: from fundamentals to applications," Nanophotonics **7**, 1169–1190 (2018).
41. G. Zheng, H. Mühlenbernd, M. Kenney, *et al.*, "Metasurface holograms reaching 80% efficiency," Nat. Nanotechnol. **10**, 308–312 (2015).
42. W. Wan, J. Gao, and X. Yang, "Metasurface holograms for holographic imaging," Adv. Opt. Mater. **5**, 1700541 (2017).
43. V. A. Bushuev, D. M. Tsvetkov, V. V. Konotop, *et al.*, "Unidirectional invisibility and enhanced reflection of short pulses in quasi-PT-symmetric media," Opt. Lett. **44**, 5667–5670 (2019).
44. D. M. Tsvetkov, V. A. Bushuev, V. V. Konotop, *et al.*, "Broadband quasi-PT-symmetry sustained by inhomogeneous broadening of the spectral line," Phys. Rev. A **98**, 053844 (2018).
45. X. Ni, Z. J. Wong, M. Mrejen, *et al.*, "An ultrathin invisibility skin cloak for visible light," Science **349**, 1310–1314 (2015).
46. N. Wu, Y. Jia, C. Qian, *et al.*, "Pushing the limits of metasurface cloak using global inverse design," Adv. Opt. Mater. **11**, 2202130 (2023).
47. M. M. Sadafi, M. Taghavi, A. F. da Mota, *et al.*, "Optical manipulation of nanoparticles: a selective excitation approach using highly focused orbital angular momentum beams," Adv. Photonics Res. **4**, 2200224 (2023).
48. M. Taghavi and H. Mosallaei, "Increasing the stability margins using multi-pattern metasails and multi-modal laser beams," Sci. Rep. **12**, 20034 (2022).
49. A. Salandrino, S. Fardad, and D. N. Christodoulides, "Generalized Mie theory of optical forces," J. Opt. Soc. Am. B **29**, 855–866 (2012).
50. M. Taghavi, M. M. Salary, and H. Mosallaei, "Multifunctional metasails for self-stabilized beam-riding and optical communication," Nanoscale Adv. **4**, 1727–1740 (2022).
51. J. Gao, C. Lan, Q. Zhao, *et al.*, "Experimental realization of Mie-resonance terahertz absorber by self-assembly method," Opt. Express **26**, 13001–13011 (2018).
52. J. Tian, Q. Li, P. A. Belov, *et al.*, "High-*Q* all-dielectric metasurface: super and suppressed optical absorption," ACS Photonics **7**, 1436–1443 (2020).
53. J. Gao, C. Lan, Q. Zhao, *et al.*, "Electrically controlled Mie-resonance absorber," Opt. Express **25**, 22658–22666 (2017).
54. M. M. Sadafi, H. Karami, and M. Hosseini, "A tunable hybrid graphene-metal metamaterial absorber for sensing in the THz regime," Curr. Appl. Phys. **31**, 132–140 (2021).
55. G. Li, S. Zhang, and T. Zentgraf, "Nonlinear photonic metasurfaces," Nat. Rev. Mater. **2**, 17010 (2017).
56. A. Krasnok, M. Tymchenko, and A. Alù, "Nonlinear metasurfaces: a paradigm shift in nonlinear optics," Mater. Today **21**, 8–21 (2018).
57. A. Zalogina, L. Carletti, A. Rudenko, *et al.*, "High-harmonic generation from a subwavelength dielectric resonator," Sci. Adv. **9**, eadg2655 (2023).
58. P. Vabishchevich and Y. Kivshar, "Nonlinear photonics with metasurfaces," Photonics Res. **11**, B50–B64 (2023).
59. J. Gao, M. A. Vincenti, J. Frantz, *et al.*, "All-optical tunable wavelength conversion in opaque nonlinear nanostructures," Nanophotonics **11**, 4027–4035 (2022).
60. J. Gao, M. A. Vincenti, J. Frantz, *et al.*, "Near-infrared to ultra-violet frequency conversion in chalcogenide metasurfaces," Nat. Commun. **12**, 5833 (2021).
61. N. I. Zheludev and D. Wilkowski, "The rise of toroidal electrodynamics and spectroscopy," ACS Photonics **10**, 556–558 (2023).
62. A. Ahmadivand, B. Gerislioglu, R. Ahuja, *et al.*, "Toroidal metaphotonics and metadevices," Laser Photonics Rev. **14**, 1900326 (2020).
63. N. Talebi, S. Guo, and P. A. van Aken, "Theory and applications of toroidal moments in electrodynamics: their emergence, characteristics, and technological relevance," Nanophotonics **7**, 93–110 (2018).
64. I. Fernandez-Corbaton, S. Nanz, and C. Rockstuhl, "On the dynamic toroidal multipoles from localized electric current distributions," Sci. Rep. **7**, 7527 (2017).
65. A. C. Valero, D. Borovkov, M. Sidorenko, *et al.*, "On the existence of pure, broadband toroidal sources in electrodynamics," arXiv, arXiv:2208.02908 (2022).
66. G. Gbur and E. Wolf, "Nonradiating sources and other 'invisible' objects," in *Progress in Optics* (2003), Vol. **45**, pp. 273–316.
67. K. Kim and E. Wolf, "Non-radiating monochromatic sources and their fields," Opt. Commun. **59**, 1–6 (1986).
68. G. N. Afanasiev and Y. P. Stepanovsky, "The electromagnetic field of elementary time-dependent toroidal sources," J. Phys. A **28**, 4565 (1995).
69. A. Mirzaei, A. E. Miroshnichenko, I. V. Shadrivov, *et al.*, "Superscattering of light optimized by a genetic algorithm," Appl. Phys. Lett. **105**, 011109 (2014).
70. Z. Ruan and S. Fan, "Superscattering of light from subwavelength nanostructures," Phys. Rev. Lett. **105**, 013901 (2010).
71. Y. Huang and L. Gao, "Superscattering of light from core–shell nonlocal plasmonic nanoparticles," J. Phys. Chem. C **118**, 30170–30178 (2014).
72. S. Lepeshov, A. Krasnok, and A. Alú, "Nonscattering-to-superscattering switch with phase-change materials," ACS Photonics **6**, 2126–2132 (2019).
73. C. Qian, X. Lin, Y. Yang, *et al.*, "Experimental observation of superscattering," Phys. Rev. Lett. **122**, 063901 (2019).
74. W. Liu, "Superscattering pattern shaping for radially anisotropic nanowires," Phys. Rev. A **96**, 023854 (2017).
75. D. Vercruysse, Y. Sonnefraud, N. Verellen, *et al.*, "Unidirectional side scattering of light by a single-element nanoantenna," Nano Lett. **13**, 3843–3849 (2013).
76. B. Ng, J. Wu, S. M. Hanham, *et al.*, "Spoof plasmon surfaces: a novel platform for THz sensing," Adv. Opt. Mater. **1**, 543–548 (2013).
77. S. Zeng, D. Baillargeat, H.-P. Hod, *et al.*, "Nanomaterials enhanced surface plasmon resonance for biological and chemical sensing applications," Chem. Soc. Rev. **43**, 3426–3452 (2014).
78. V. I. Shcherbinin, V. I. Fesenko, T. I. Tkachova, *et al.*, "Superscattering from subwavelength corrugated cylinders," Phys. Rev. Appl. **13**, 024081 (2020).
79. K. Asham, I. Al-Ani, L. Huang, *et al.*, "Boosting strong coupling in a hybrid WSe_2 monolayer–anapole–plasmon system," ACS Photonics **8**, 489–496 (2021).
80. J. Wang, W. Yang, G. Sun, *et al.*, "Boosting anapole-exciton strong coupling in all-dielectric heterostructures," Photonics Res. **10**, 1744–1753 (2022).

81. G. Grinblat, Y. Li, M. P. Nielsen, *et al.*, "Enhanced third harmonic generation in single germanium nanodisks excited at the anapole mode," Nano Lett. **16**, 4635–4640 (2016).
82. L. Xu, M. Rahmani, K. Z. Kamali, *et al.*, "Boosting third-harmonic generation by a mirror-enhanced anapole resonator," Light Sci. Appl. **7**, 44 (2018).
83. G. Grinblat, Y. Li, M. P. Nielsen, *et al.*, "Efficient third harmonic generation and nonlinear subwavelength imaging at a higher-order anapole mode in a single germanium nanodisk," ACS Nano **11**, 953–960 (2017).
84. Y. Li, Z. Huang, Z. Sui, *et al.*, "Optical anapole mode in nanostructured lithium niobate for enhancing second harmonic generation," Nanophotonics **9**, 3575–3585 (2020).
85. K.-H. Kim and W.-S. Rim, "Anapole resonances facilitated by high-index contrast between substrate and dielectric nanodisk enhance vacuum ultraviolet generation," ACS Photonics **5**, 4769–4775 (2018).
86. D. G. Baranov, R. Verre, P. Karpinski, *et al.*, "Anapole-enhanced intrinsic Raman scattering from silicon nanodisks," ACS Photonics **5**, 2730–2736 (2018).
87. M. Ghahremani, M. K. Habil, and C. J. Zapata-Rodriguez, "Anapole-assisted giant electric field enhancement for surface-enhanced coherent anti-Stokes Raman spectroscopy," Sci. Rep. **11**, 10639 (2021).
88. T. Zhang, Y. Che, K. Chen, *et al.*, "Anapole mediated giant photothermal nonlinearity in nanostructured silicon," Nat. Commun. **11**, 3027 (2020).
89. T. Huang, B. Wang, W. Zhang, *et al.*, "Ultracompact energy transfer in anapole-based metachains," Nano Lett. **21**, 6102–6110 (2021).
90. V. Mazzone, J. S. T. Gongora, and A. Fratalocchi, "Near-field coupling and mode competition in multiple anapole systems," Appl. Sci. **7**, 542 (2017).
91. A. Tripathi, H.-R. Kim, P. Tonkaev, *et al.*, "Lasing action from anapole metasurfaces," Nano Lett. **21**, 6563–6568 (2021).
92. B. Luk'yanchuk, R. Paniagua-Domínguez, A. I. Kuznetsov, *et al.*, "Hybrid anapole modes of high-index dielectric nanoparticles," Phys. Rev. A **95**, 063820 (2017).
93. E. A. Gurvitz, K. S. Ladutenko, P. A. Dergachev, *et al.*, "The high-order toroidal moments and anapole states in all-dielectric photonics," Laser Photonics Rev. **13**, 1800266 (2019).
94. A. C. Valero, E. A. Gurvitz, F. A. Benimetskiy, *et al.*, "Theory, observation, and ultrafast response of the hybrid anapole regime in light scattering," Laser Photonics Rev. **15**, 2100114 (2021).
95. A. K. Ospanova, A. Basharin, A. E. Miroshnichenko, *et al.*, "Generalized hybrid anapole modes in all-dielectric ellipsoid particles," Opt. Mater. Express **11**, 23–34 (2021).
96. A. A. Basharin, E. Zanganeh, A. K. Ospanova, *et al.*, "Selective superinvisibility effect via compound anapole," Phys. Rev. B **107**, 155104 (2023).
97. A. V. Kuznetsov, A. C. Valero, H. K. Shamkhi, *et al.*, "Special scattering regimes for conical all-dielectric nanoparticles," Sci. Rep. **12**, 21904 (2022).
98. R. Alaee, C. Rockstuhl, and I. Fernandez-Corbaton, "An electromagnetic multipole expansion beyond the long-wavelength approximation," Opt. Commun. **407**, 17–21 (2018).
99. A. B. Evlyukhin, T. Fischer, C. Reinhardt, *et al.*, "Optical theorem and multipole scattering of light by arbitrarily shaped nanoparticles," Phys. Rev. B **94**, 205434 (2016).
100. A. B. Evlyukhin and B. N. Chichkov, "Multipole decompositions for directional light scattering," Phys. Rev. B **100**, 125415 (2019).
101. J. D. Jackson, *Classical Electrodynamics* (Wiley, 1998), pp. 841–842.
102. A. B. Evlyukhin, C. Reinhardt, and B. N. Chichkov, "Multipole light scattering by nonspherical nanoparticles in the discrete dipole approximation," Phys. Rev. B **84**, 235429 (2011).
103. P. Lalanne, W. Yan, K. Vynck, *et al.*, "Light interaction with photonic and plasmonic resonances," Laser Photonics Rev. **12**, 1700113 (2018).
104. T. Wu, D. Arrivault, W. Yan, *et al.*, "Modal analysis of electromagnetic resonators: user guide for the man program," Comput. Phys. Commun. **284**, 108627 (2023).
105. M. A. Vincenti, J. Gao, D. de Ceglia, *et al.*, "Stacked chalcogenide metasurfaces for third harmonic generation in the UV range," New J. Phys. **24**, 035005 (2022).
106. P. R. Sharapova, S. S. Kruk, and A. S. Solntsev, "Nonlinear dielectric nanoresonators and metasurfaces: toward efficient generation of entangled photons," Laser Photonics Rev. **17**, 2200408 (2023).
107. S. Lepeshov, A. Vyshnevyy, and A. Krasnok, "Switchable dual-mode nanolaser: mastering emission and invisibility through phase transition materials," Nanophotonics **12**, 3729–3736 (2023).
108. L. Kang, R. P. Jenkins, and D. H. Werner, "Recent progress in active optical metasurfaces," Adv. Opt. Mater. **7**, 1801813 (2019).
109. T. Cui, B. Bai, and H.-B. Sun, "Tunable metasurfaces based on active materials,"; Adv. Funct. Mater. **29**, 1806692 (2019).
110. F. Monticone, D. Sounas, A. Krasnok, *et al.*, "Can a nonradiating mode be externally excited? Nonscattering states versus embedded eigenstates," ACS Photonics **6**, 3108–3114 (2019).
111. E. Takou, A. C. Tasolamprou, O. Tsilipakos, *et al.*, "Dynamic anapole in metasurfaces made of sculptured cylinders," Phys. Rev. B **100**, 085431 (2019).
112. S. E. Svyakhovskiy, V. V. Ternovski, and M. I. Tribelsky, "Anapole: its birth, life, and death," Opt. Express **27**, 23894–23904 (2019).
113. M. I. Tribelsky and A. E. Miroshnichenko, "Two tractable models of dynamic light scattering and their application to Fano resonances," Nanophotonics **10**, 4357–4371 (2021).
114. H. B. Sedeh, D. Pires, N. Chandra, *et al.*, "Manipulation of scattering spectra with topology of light and matter," Laser Photonics Rev. **17**, 2200472 (2023).
115. V. R. Tuz, V. Dmitriev, and A. B. Evlyukhin, "Antitoroidic and toroidic orders in all-dielectric metasurfaces for optical near-field manipulation," ACS Appl. Nano Mater. **3**, 11315–11325 (2020).
116. R. E. Raab and O. L. De Lange, "Comment on 'On the origin dependence of multipole moments in electromagnetism,';" J. Phys. D **43**, 508001 (2010).
117. V. Dmitriev, S. D. S. Santos, A. B. Evlyukhin, *et al.*, "Toroidic and antitoroidic orders in hexagonal arrays of dielectric trimers: magnetic group approach," Phys. Rev. B **103**, 165402 (2021).
118. A. Ospanova, M. Cojocari, and A. Basharin, "Modified multipoles in photonics," Phys. Rev. B **107**, 035156 (2023).
119. S. Tian, J. Wang, S. Sun, *et al.*, "The anapole state excited by an oblique incidence," Phys. Scr. **98**, 085515 (2023).
120. E. Díaz-Escobar, T. Bauer, E. Pinilla-Cienfuegos, *et al.*, "Radiationless anapole states in on-chip photonics," Light Sci. Appl. **10**, 204 (2021).
121. E. Díaz-Escobar, Á. I. Barreda, A. Griol, *et al.*, "Experimental observation of higher-order anapoles in individual silicon disks under in-plane illumination," Appl. Phys. Lett. **121**, 201105 (2022).
122. M. Poleva, K. Frizyuk, K. Baryshnikova, *et al.*, "Multipolar theory of bianisotropic response of meta-atoms," Phys. Rev. B **107**, L041304 (2023).
123. A. C. Valero, H. K. Shamkhi, A. S. Kupriianov, *et al.*, "Superscattering emerging from the physics of bound states in the continuum," Nat. Commun. **14**, 4689 (2023).
124. M. F. Limonov, M. V. Rybin, A. N. Poddubny, *et al.*, "Fano resonances in photonics," Nat. Photonics **11**, 543–554 (2017).
125. E. Melik-Gaykazyan, K. Koshelev, J.-H. Choi, *et al.*, "From Fano to quasi-BIC resonances in individual dielectric nanoantennas," Nano Lett. **21**, 1765–1771 (2021).
126. M. V. Rybin, K. B. Samusev, I. S. Sinev, *et al.*, "Mie scattering as a cascade of Fano resonances," Opt. Express **21**, 30107–30113 (2013).
127. V. A. Zenin, A. B. Evlyukhin, S. M. Novikov, *et al.*, "Direct amplitude-phase near-field observation of higher-order anapole states," Nano Lett. **17**, 7152–7159 (2017).